

AD-A085 083

FRANK J SEILER RESEARCH LAB UNITED STATES AIR FORCE A--ETC F/6 20/4
AN INVESTIGATION OF UNSTEADY FLOW SEPARATION.(U)

MAR 80 M S FRANCIS, J E KEESEE, J P RETELLE

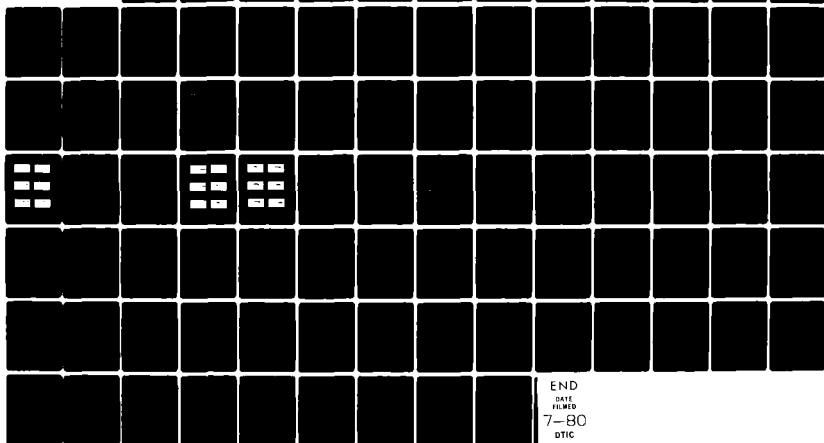
UNCLASSIFIED

SRL-TR-80-0009

NL

For 1

950-83



END
DATE
FILMED
7-80
DTIC

② LEVEL II



FRANK J. SEILER RESEARCH LABORATORY

SRL-TR-80-0009

MARCH 1980

AN INVESTIGATION OF UNSTEADY FLOW SEPARATION

FINAL REPORT

DTIC
ELECTE
JUN 5 1980
S B D

CAPT M. S. FRANCIS
CAPT J. E. KEESEE
MAJ J. P. RETELLE
CAPT G. E. SISSON
LT COL J. D. LANG

APPROVED FOR PUBLIC RELEASE;
DISTRIBUTION UNLIMITED.

PROJECT 2307



AIR FORCE SYSTEMS COMMAND

UNITED STATES AIR FORCE

80 5 23 010

ADA085083

FJSRL-TR-80-0009

This document was prepared by the Mechanics Division, Directorate of Aerospace-Mechanics Sciences, Frank J. Seiler Research Laboratory, United States Air Force Academy, Colorado. The research was conducted under Project Work Unit Number 2307-F1-34, An Investigation of the Flow Dynamics of Unsteady Separated Regions. Capt Michael S. Francis was the Project Engineer in charge of the work.

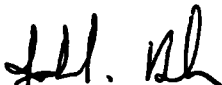
When U.S. Government drawings, specifications or other data are used for any purpose other than a definitely related Government procurement operation, the Government thereby incurs no responsibility nor any obligation whatsoever, and the fact that the Government may have formulated, furnished or in any way supplied the said drawings, specifications or other data is not to be regarded by implication or otherwise, as in any manner licensing the holder or any other person or corporation or conveying any rights or permission to manufacture, use or sell any patented invention that may in any way be related thereto.

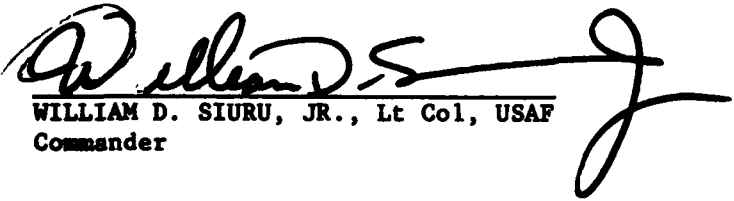
Inquiries concerning the technical content of this document should be addressed to the Frank J. Seiler Research Laboratory (AFSC), FJSRL/NH, USAF Academy, Colorado 80840. Phone AC 303-472-3122.

This report has been reviewed by the Commander and is releasable to the National Technical Information Service (NTIS). At NTIS it will be available to the general public, including foreign nations.

This technical report has been reviewed and is approved for publication.


MICHAEL S. FRANCIS, Capt, USAF
Project Engineer


JOHN S. BRUSH, Lt Col, USAF
Director
Aerospace-Mechanics Sciences


WILLIAM D. SIURU, JR., Lt Col, USAF
Commander

Copies of this report should not be returned unless return is required by security considerations, contractual obligations, or notice on a specific document.

Printed in the United States of America. Qualified requestors may obtain additional copies from the Defense Documentation Center. All others should apply to: National Technical Information Service
5285 Port Royal Road
Springfield, Virginia 22161

UNCLASSIFIED

SECURITY CLASSIFICATION OF THIS PAGE (When Data Entered)

REPORT DOCUMENTATION PAGE		READ INSTRUCTIONS BEFORE COMPLETING FORM
1. REPORT NUMBER 14 SRL-TR-80-0009 / AD A-	2. GOVT ACCESSION NO. AD-A085083	3. RECIPIENT'S CATALOG NUMBER
4. TITLE (and Subtitle) 6 AN INVESTIGATION OF UNSTEADY FLOW SEPARATION,		5. TYPE OF REPORT & PERIOD COVERED 9 Final Rept. Sep 75 - Sep 79
7. AUTHOR(s) 10 M. S. Francis J. E. Keesee J. P. Retelle		8. CONTRACT OR GRANT NUMBER(s) 12 911
9. PERFORMING ORGANIZATION NAME AND ADDRESS Frank J. Seiler Research Lab (AFSC) USAF Academy, Colorado 80840		10. PROGRAM ELEMENT, PROJECT, TASK AREA & WORK UNIT NUMBERS 16 DRS 61102F 2307-F1-34 17 FL
11. CONTROLLING OFFICE NAME AND ADDRESS Frank J. Seiler Research Lab (AFSC) USAF Academy, Colorado 80840		12. REPORT DATE 11 Mar 80
14. MONITORING AGENCY NAME & ADDRESS (if different from Controlling Office)		13. NUMBER OF PAGES 87
		15. SECURITY CLASS. (of this report) UNCLASSIFIED
16. DISTRIBUTION STATEMENT (of this Report) Approved for public release; distribution unlimited		15a. DECLASSIFICATION/DOWNGRADING SCHEDULE
17. DISTRIBUTION STATEMENT (of the abstract entered in Block 20, if different from Report)		
18. SUPPLEMENTARY NOTES		
19. KEY WORDS (Continue on reverse side if necessary and identify by block number)		
20. ABSTRACT (Continue on reverse side if necessary and identify by block number) The results of experiments in which an unsteady separated flow was generated on the surface of an airfoil immersed in an incompressible freestream are discussed. Measurements of the velocity and vorticity fields and the surface pressure distribution generated by oscillations of a fence-type spoiler located on one surface of the airfoil has confirmed the presence of a dynamically evolving vortex-like structure bearing a close resemblance to the one encountered in classical dynamic stall. The growth and development of the shear layer region is characterized through iso-vorticity contour maps at select		

DD FORM 1 JAN 73 1473

EDITION OF 1 NOV 65 IS OBSOLETE

UNCLASSIFIED

SECURITY CLASSIFICATION OF THIS PAGE (When Data Entered)

329920

UNCLASSIFIED

SECURITY CLASSIFICATION OF THIS PAGE(When Data Entered)

20. Abstract (continued)

phase points during the motion cycle. A detailed description of flow field behavior is provided over a range of dimensionless spoiler frequencies and freestream Reynolds numbers. The correlation of these results with corresponding surface pressure measurements is also presented.

ACCESSION for	
NTIS	White Section <input checked="" type="checkbox"/>
DDC	Buff Section <input type="checkbox"/>
UNANNOUNCED	<input type="checkbox"/>
JUSTIFICATION _____	
BY _____	
DISTRIBUTION/AVAILABILITY CODES	
Dist.	AvAIL. and/or SPECIAL
A	

UNCLASSIFIED

SECURITY CLASSIFICATION OF THIS PAGE(When Data Entered)

TABLE OF CONTENTS

	<u>Page</u>
NOMENCLATURE	2
LIST OF FIGURES.	3
INTRODUCTION	5
EXPERIMENTAL CONFIGURATION AND APPARATUS	8
A. General Considerations.	8
B. USAFA Wind Tunnel Experiments	9
C. Water Tunnel Flow Visualization	20
D. Measurement Conditions.	21
EXPERIMENTAL METHODS	22
A. Averaging Technique	22
B. Vorticity Measurement Technique	27
C. Sources of Error.	30
EXPERIMENTAL RESULTS	33
A. Steady Flow Description	33
B. Effects of Spoiler Oscillation at Low Reynolds Numbers.	36
C. Unsteady Flow at High Reynolds Numbers.	39
D. Unsteady Vorticity Field in the Outer Shear Layer	39
E. Vortex Growth Characteristics	46
F. Vorticity Field Correlation with Surface Pressure Field	53
G. Flow Near the Airfoil Surface	59
H. Turbulence Intensities.	74
SUMMARY.	83
ACKNOWLEDGEMENTS	85
REFERENCES	86

NOMENCLATURE

C_p	pressure coefficient, based on freestream dynamic pressure, $\frac{P-P_\infty}{\frac{1}{2}\rho U_\infty^2}$
Re	Reynolds number based on freestream velocity and airfoil chord, $\frac{U_\infty c}{\nu}$
U_c	characteristic growth velocity of the separated region in the freestream direction
U_∞	freestream velocity
c	airfoil chord length
h_s	instantaneous spoiler height, maximum value given by $h_{s_{max}}$
k	dimensionless frequency based on airfoil semi-chord, $\frac{\omega c}{2U_\infty}$
t	time
\vec{u}	flow velocity vector, $\vec{u} = u\hat{i} + v\hat{j} + w\hat{k}$
\vec{x}	position vector, $\vec{x} = x\hat{i} + y\hat{j} + z\hat{k}$
Γ	circulation around a closed contour, C
α	airfoil angle of attack
δ	"X"-configuration hot-film probe crossflow angle
$\vec{\xi}$	vorticity vector, $\vec{\xi} = \xi_x\hat{i} + \xi_y\hat{j} + \xi_z\hat{k}$ (a prime denotes dimensionless form)
ϕ	spoiler oscillation phase angle ($\phi = \omega t$)
ω	spoiler oscillation frequency (radians/sec)
$\langle \rangle$	brackets denote a spatial average

LIST OF FIGURES

	<u>Page</u>
Figure 1. Functional Schematic of Experimental Apparatus	12
Figure 2. Analog Linearizer Schematic - Output - $E_L = [G(E_{hw}^2 - E_{hwo}^2)]^n$	14
Figure 3. Traversing Mechanism - Position Monitor Amplifier Circuit (Single Channel)	15
Figure 4. LDV Optical Arrangement.	17
Figure 5. LDV Optical System and Wind Tunnel Test Section.	19
Figure 6. Algorithm Incorporating Total Velocity Vector (Residence Time) Bias Correction.	24
Figure 7. Contour Array Geometry - Outer Shear Layer	29
Figure 8. Flow Regions During Separation Process	31
Figure 9. Iso-vorticity Contours Associated with Steady Flow Separation, Spoiler Fully Extended, $Re = 287,000$ ($U_\infty = 70$ ft/sec)	35
Figure 10. Unsteady Separation at Low Reynolds Number, $k = 3.70$, $Re = 10,000$	37
Figure 11. Unsteady Separation at High Reynolds Number, $k = 0.85$, $Re = 246,000$	40
Figure 12. Iso-vorticity Contours Associated with Unsteady Flow Separation, $k = 1.2$, $Re = 180,000$ ($U_\infty = 60$ ft/sec)	42
Figure 13. Iso-vorticity Contours Associated with Unsteady Flow Separation, $k = 0.2$, $Re = 287,000$ ($U_\infty = 70$ ft/sec)	44
Figure 14. Iso-vorticity Contours in the Outer Shear Layer - Negative Vorticity	47
Figure 15. Length of the Separated Region as a Function of Phase Angle.	50
Figure 16. Characteristic Vortex Growth Velocity - Frequency Variation.	52
Figure 17. Maximum Value of Laterally-Averaged Vorticity as Function of Reynolds Number	54
Figure 18. Minimum Pressure Coefficient Variation with Frequency.	55
Figure 19. Comparison of Pressure Distribution and Laterally-Averaged Vorticity.	57

	<u>Page</u>
Figure 20. Length of Separation Zone - Comparison, $Re = 410,000$, $k = 0.5$	58
Figure 21. Freestream Velocity Component Profiles Obtained with Laser Doppler Velocimeter, $k = 0.2$, $U_{\infty} = 70$ ft/sec	60
Figure 22. Freestream Velocity Component Profiles Obtained with Laser Doppler Velcoimeter, $k = 0.85$, $U_{\infty} = 60$ ft/sec.	63
Figure 23. Freestream Velocity Component Flow Reversal Envelope, $k = 0.2$, $U_{\infty} = 70$ ft/sec.	68
Figure 24. Freestream Velocity Component Flow Reversal Envelope, $k = 0.85$, $U_{\infty} = 60$ ft/sec	69
Figure 25. Freestream Velocity Component Flow Reversal - Phase History, $k = 0.2$, $U_{\infty} = 70$ ft/sec.	70
Figure 26. Freestream Velocity Component Flow Reversal - Phase History, $k = 0.85$, $U_{\infty} = 60$ ft/sec	71
Figure 27. Comparison of Velocity Component Values in the Freestream Direction.	72
Figure 28. Freestream Velocity Component - Turbulence Intensity Profiles, $k = 0.2$, $U_{\infty} = 70$ ft/sec.	75
Figure 29. Freestream Velocity Component - Turbulence Intensity Profiles, $k = 0.85$, $U_{\infty} = 60$ ft/sec	77
Figure 30. Maximum Turbulence Intensities - Phase Histories, $k = 0.2$, $U_{\infty} = 70$ ft/sec	81
Figure 31. Maximum Turbulence Intensities - Phase Histories, $k = 0.85$, $U_{\infty} = 60$ ft/sec	82

INTRODUCTION

Flow separation and reattachment are physical phenomena that must be confronted in a wide variety of engineering problems. They frequently pose a serious obstacle toward the attainment of a satisfactory prediction of overall flow field behavior because of the analytical complexity arising from the interaction of the various dominant physical mechanisms. These problems become even more complicated when nonstationarity of the mean flow field must be considered.

While many negative features associated with flow separation are well documented for a wide variety of engineering applications, the potential for exploiting favorable aspects of energetic unsteady separation has only recently received attention. It is known that during rapid high-g flight vehicle maneuvers at high angles of attack, complex aerodynamic phenomena such as dynamic stall (involving time-varying flow separation) may occur resulting in aerodynamic loads which differ significantly from those predicted using steady flow considerations. Large excursions in the lift coefficient caused by energetic, stable separation vortices and ranging well in excess of the maximum steady flow value might well be exploited for productive application. Future designs of advanced maneuverable flight vehicles, both manned and unmanned, may well seek to incorporate these advantageous effects in a constructive manner to enlarge the effective flight envelope. The capability to produce controlled flow behavior necessary for these improvements must be preceded by a more complete knowledge of the mechanics of unsteady separation in general.

Numerous investigators have chronicled their research efforts in unsteady separated flows. An excellent early survey of the progress in this area can be found in the text by Chang.¹ Problems associated with

various forms of unsteady separation have been recognized and studied for some time, ranging from shock wave-boundary layer interaction encountered in high speed flight^{2,3} to the understanding of lift generation mechanisms for various forms of insect life.^{4,5} Another phenomenon of recent interest exhibiting global unsteady separation caused by the pitching motion of an airfoil is that of dynamic stall.⁶⁻¹¹ A comprehensive review of progress on many of the problems involving unsteady separation can be obtained from recent articles by McCroskey.^{12,13}

The discussion which follows is directed toward a realistic characterization of a flow involving controlled unsteady separation. An experiment was devised employing an airfoil having an oscillating fence-type spoiler located at mid-chord on one surface which was immersed in a subsonic wind tunnel freestream. With a capability to adjust spoiler oscillation amplitude and frequency, this configuration provided for limited control of the size of the separated region while fixing the separation point with respect to the freestream coordinate direction. The resulting two-dimensional mean flow geometry greatly reduced the quantity of measurements necessary to characterize the flow field and surface loading parameters. Another major advantage of this particular configuration was the extensive data base available from previous investigations of flows with similar geometries.¹⁴⁻¹⁶

Coincident with the search for a generalized separation zone geometry was the selection of a method for characterizing the detailed nature of this rather complex flow field. Available evidence from similar studies¹¹ pointing to the presence of vortex-like structures suggested vorticity as a logical choice for a characterization variable. Not only does the use of this parameter provide a method of reconstructing the velocity field if desired, but it identifies those regions where real fluid effects, e.g.,

viscosity, are prevalent. An additional benefit of this representation in the present case becomes apparent if one realizes that, in two-dimensional flow, an assessment of the distribution of the mean vorticity component orthogonal to the plane of flow will provide a scalar field representation of the flow. Since only one component of vorticity is required, the degree of complexity in "measuring" the flow is greatly diminished.

Early research by the authors^{17,18} resulted in the development of a semi-empirical model of unsteady separation verified with surface pressure field measurements exclusively. Experimental results confirmed the existence of both a lag in the growth of the separated region and an overshoot in the steady flow pressure which were the model's essential features. The most questionable aspect of that analysis involved the potential of extending the model beyond its assumed limits, i.e., small perturbations and high aspect ratio separated region geometry, factors which are related to the accuracy of the flow field description itself. The model was predicated on the concept of a growing and shrinking separation "bubble" - a feature which has not been verified in the case of large overwhelming perturbations as in the experiments described below.

The objective of this investigation, then, was to describe and discuss the behavior of unsteady flow separation associated with this geometry and to correlate it with the resulting surface pressure distribution. Among the significant parameters varied were the Reynolds number and the dimensionless frequency, with steady flow results included for comparison. Measurements of the global ensemble-averaged vorticity field resulting from simple harmonic spoiler oscillations have verified that the separation zone is not merely a growing and shrinking "bubble" as previously conceptualized, but is a dynamically evolving vortex-like structure bearing a strong resemblance to the one encountered in the dynamic stall flow field.

EXPERIMENTAL CONFIGURATION AND APPARATUS

A. General Considerations

To provide limited control of the region of unsteady separation, an experiment was devised employing an airfoil with an oscillating fence-type spoiler located at mid-chord on one surface. This configuration allowed for the variation of separation zone geometry parameters through preset adjustments of spoiler mean height and amplitude, while the oscillation frequency could be varied continuously. During the initial design, it was thought that the airfoil angle of attack could serve to control the boundary layer upstream of the spoiler. It was subsequently discovered that the interaction between the upstream attached boundary layer and the downstream separation zone was minimal while the airfoil was symmetrically oriented with respect to the freestream direction ($\alpha = 0^\circ$). The NACA 0012 airfoil employed in this investigation also proved useful due to the extensive data base available from previous investigations of flows using this particular shape.

Experiments were conducted under incompressible freestream conditions with the Reynolds number ranging from approximately 1×10^4 to a maximum value of 5.5×10^5 . Two geometrically similar models were employed in contrasting flow environments. A series of wind tunnel experiments in which both surface pressures and flow field characteristics were assessed in detail were supplemented by corresponding experiments in low speed water tunnel for purposes of flow visualization. While the wind tunnel results provide the majority of data presented in this report, the water tunnel measurements served a useful purpose in identifying those spatial regions during the motion cycle where the various measurement techniques might be subject to excessive error or other limitations. In addition, these results

provided for a qualitative assessment of the global flow field independent of the wind tunnel measurements.

B. USAFA Wind Tunnel Experiments

An extensive series of experiments were conducted in the USAF Academy 0.61 m x 0.91 m (2 ft x 3 ft) subsonic wind tunnel facility.¹⁹ The airfoil model was constructed with a 25.4 cm (10 inch) chord and configured so that it spanned the tunnel across the shorter dimension. The model was fabricated from three fitted, solid aluminum pieces which were subsequently excavated to provide chambers for the pressure transducers, spoiler and portions of the oscillation mechanism. Positionable plexiglass endplates provided a capability to vary the aspect ratio of that portion of the airfoil over which the measurements were made. The primary purpose of the endplates was to suppress unwanted three-dimensional effects in the separated region, e.g., net axial flow in the vortex center. As a result of a preliminary survey, the endplates were fixed at a separation distance of 35.6 cm (14 inches), providing an aspect ratio of 1.4 for all measurements described in this report.

The aluminum fence-type spoiler was fabricated so that it could easily slide in a teflon-lined groove located at the mid-chord point of the airfoil. Oscillation was produced using a rack and gear arrangement located outside the wind tunnel on either side of the airfoil. Two spur gear segments were coupled by a rotating rod which extended through the airfoil at the 30% chord location. The rod was coupled to a DC motor servo-drive system using a linkage whose exclusive purpose was to produce pure sinusoidal oscillations. Resultant spoiler motion could then be described by the following equation:

$$h_s(t) = \frac{h_{s\max}}{2} (1 - \cos \omega t) \quad (1)$$

The linkage arrangement provided for the adjustment of both mean height and amplitude prior to the initiation of motion. The maximum fractional perturbation to the flow expressed as a ratio of spoiler height to wing semi-chord was equal to 0.1. The DC motor drive system (Electrocraft Model E760M) could be varied to provide oscillation frequencies from DC to 20 Hz to within 0.01 Hz resolution. This corresponded to a reduced frequency range extending from $0 \leq k < 1.2$, depending on the flow velocity. Although the DC motor drive system employed tachometer feedback for accurate constant speed control, additional damping of unwanted inertial effects in the drive linkage was provided through a heavy flywheel positioned on the motor shaft.

The instantaneous spoiler position was determined using two linear position potentiometers connected to the spanwise extremes of the spoiler outside the wind tunnel. These devices were used not only to verify the accuracy and repeatability of the motion, but also to examine the spanwise alignment of the spoiler.

A photo-optical emitter/detector circuit was used to provide a signal which was used as a phase-locked trigger source to correlate data sampling to an event associated with the periodic flow field drive, namely the spoiler position. The emitter and receiver elements were positioned on either side of a thin sheet metal disk which was fixed to the flywheel and in which a small slit had been cut. After linkage adjustment, this disk could be rotated so that the resulting pulse output of the photodetector circuit coincided with a prescribed value of the spoiler height.

An overall schematic of the experimental instrumentation is provided in Figure 1. The airfoil model was instrumented with 16 precision miniature differential pressure transducers (Kulite Model CQH140-5D) located chord-wise along its centerline. Ten of these units were located on the airfoil upper surface (same side as the spoiler) at distances of 1, 4, 25, 45, 52, 60, 70, 80, 87.5, and 93.5 percent chord behind the leading edge. The remainder were located on the airfoil lower surface at 1, 6, 30, 55, 75, and 92 percent chord. All transducers were installed so that the upper frequency limit of operation of each pressure measurement system was never lower than 400 Hz. Amplification of the pressure signals was provided by a bank of Ectron Model 562 differential amplifier units.

The central element of the instrumentation system was a Digital Equipment Corporation PDP 11/45 data acquisition system configured with a laboratory peripheral system (LPS-11) having a 24 analog channel input capacity. In addition to a capability for the automated acquisition of analog data, the system was also equipped with three digital input/output ports to be used with devices employing parallel digital signals. The system central processing unit was configured with 128k words of core memory (16 bits per word) and 20 megawords of disk storage capacity. Additional mass storage was accessible through a network link to another PDP 11 computing system having a magnetic tape drive as well as other peripherals. The laboratory peripheral system was equipped with a high speed real-time clock, multiple Schmidt triggers, relays and other hardware interface subsystems designed for use in laboratory applications.

The measurement of flow velocities associated with the separated region was accomplished with several diverse techniques.

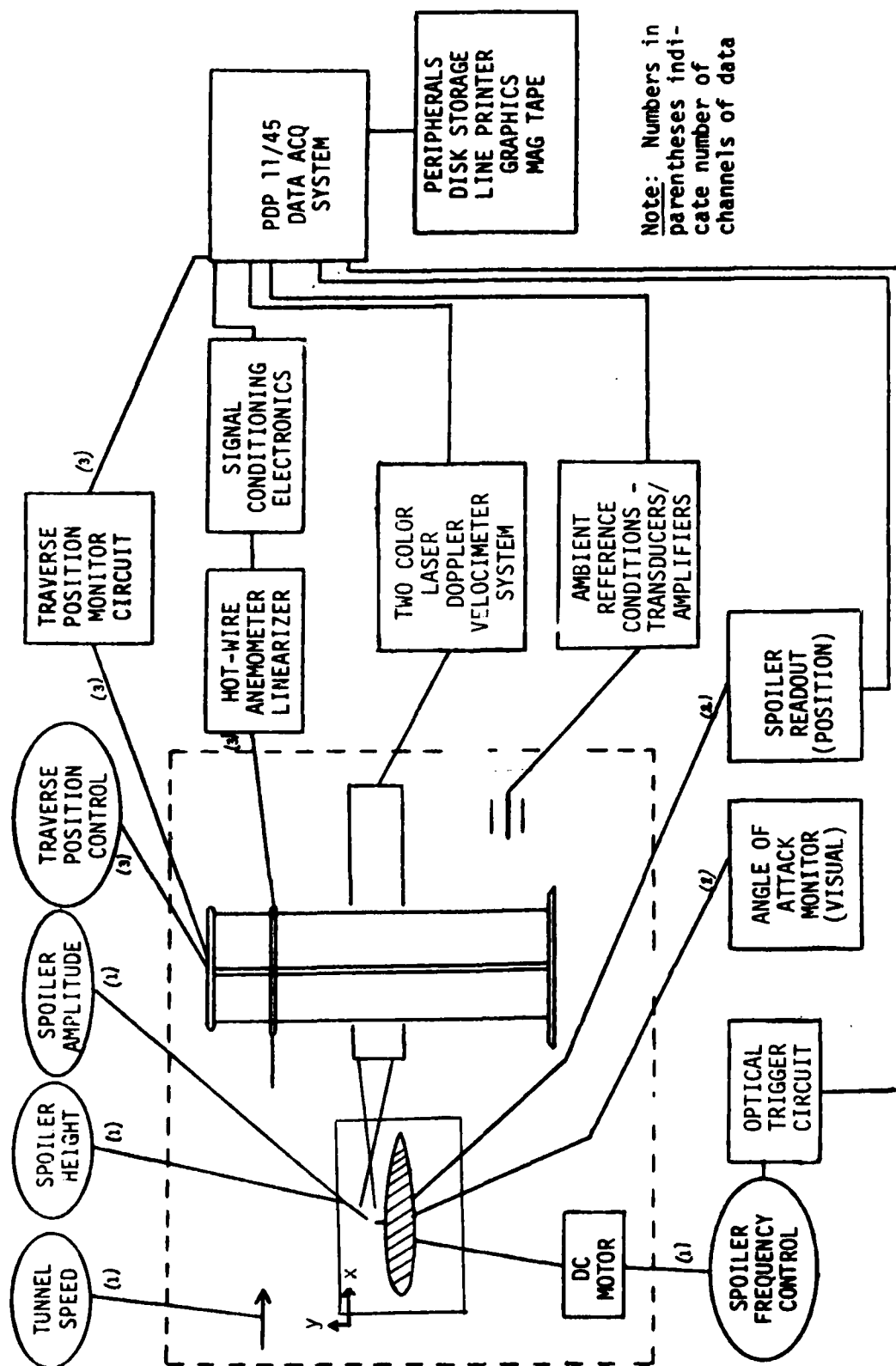
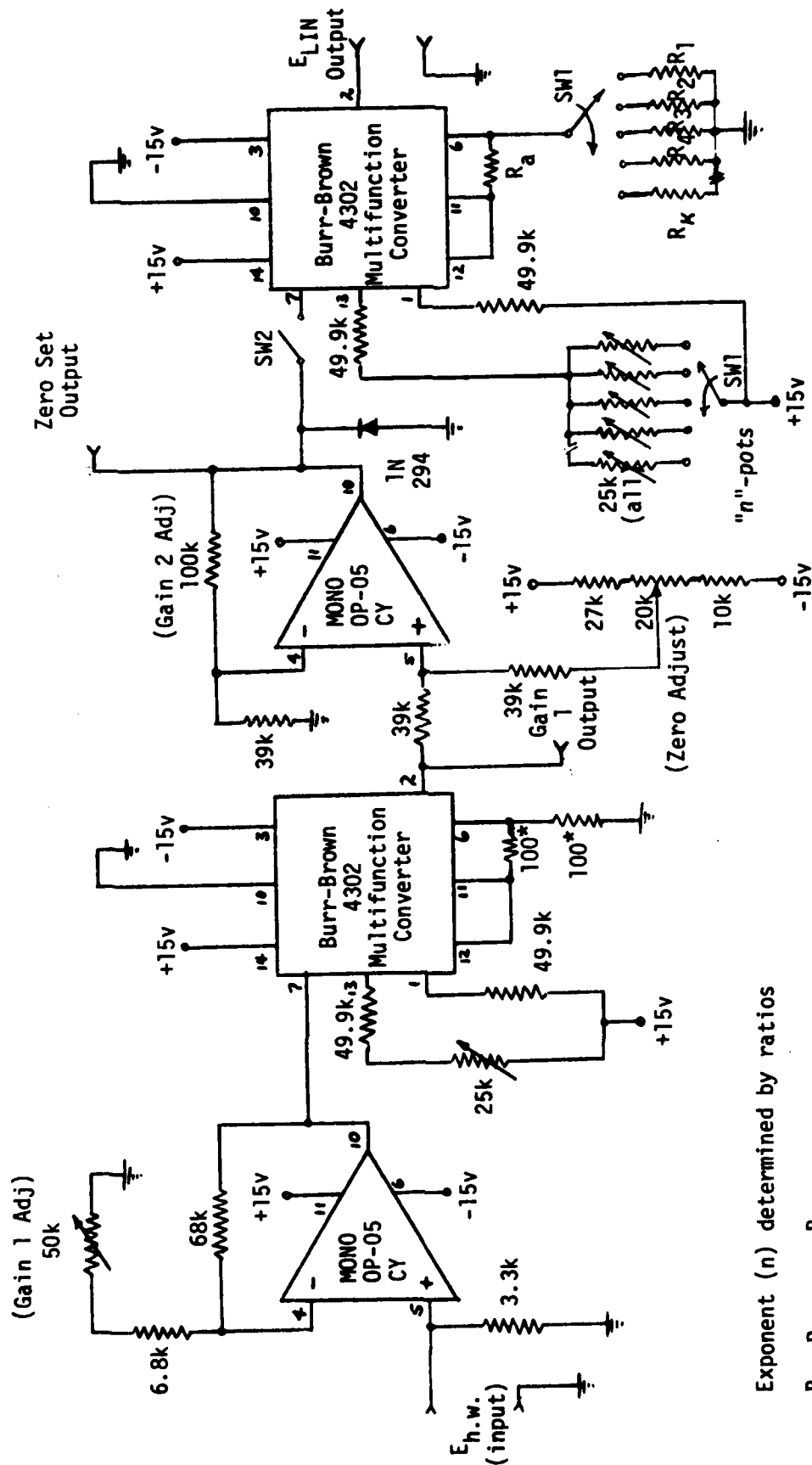


Figure 1. Functional Schematic of Experimental Apparatus

A multi-component, constant temperature, linearized hot-film anemometry system was configured with an X-geometry probe oriented to provide two orthogonal components of velocity from which the vorticity field could be inferred. TSI Model 1050 anemometer circuits were used in conjunction with readily available commercial probes. Linearization of the anemometer outputs was provided by several analog linearizers designed especially for this application. The design of these units is based on a King's Law concept resulting in maximum accuracy in air at low speeds. Figure 2 displays the circuit schematic. A primary advantage of this circuit is exceptional DC stability over long time periods - a characteristic extremely important in the present case. Additional analog signal-conditioning circuitry was used where necessary to provide output voltages which were directly proportional to the instantaneous velocity component magnitudes.

Probes were moved and accurately positioned in the wind tunnel test section using a motorized three-dimensional traversing mechanism employing orthogonal ball bearing screw drive assemblies. The system was designed so that the complete mechanical package was contained inside the tunnel test section with minimal frontal area to avoid unwanted blockage effects. Miniaturized high-torque direct current gear motors were used to turn the screw assemblies. Continuous analog position outputs were available from multi-turn, precision potentiometers appropriately geared to the drive assemblies. The simple amplifier circuit shown in Figure 3 was used to convert the instantaneous resistance ratio of each potentiometer to a voltage proportional to the probe location. Control of the miniature drive motors was achieved either manually or through an amplifier actuated by an output voltage from the digital-to-analog (D/A) converters interfaced with the data acquisition system. Position control through computer software



Exponent (n) determined by ratios

$$\frac{R_1}{R_2}, \frac{R_2}{R_3}, \dots, \frac{R_K}{R_n}, \text{ etc.}$$

Figure 2. Analog Linearizer Schematic - Output - $E_L = [G(E_{hw}^2 - E_{hw0}^2)]^n$

allowed for the complete automation of the experiment for a large array of spatial measurement locations.

Although the hot-film anemometer system described above provided a method for assessing the flow in the outer shear layer region, its application was limited near the airfoil and spoiler surfaces during portions of the cycle due to mechanical interference caused by energetic flow reversal in those regions. To provide accurate near surface flow velocity measurements, a multi-component laser Doppler velocimetry (LDV) system was developed.

Accurate velocity measurements near the airfoil surface, for both forward and reverse flows, were provided by a dual-color backscatter laser Doppler velocimeter (LDV) system. The system configuration was optimized for this experiment and was driven by data requirements and the physical constraints of the experimental apparatus. Since optical access to the wind tunnel test section was available only through a single optical-quality window, a backscatter system with a relatively high-power laser was necessary. Data requirements for two velocity components including reversed flow dictated a two-color system employing frequency shifting using Bragg cells. A four-watt (Lexel Corporation) argon-ion laser providing strong lasing lines at 4.880 nm (blue) and 5.145 nm (green) wavelengths was employed along with an integrated optical system manufactured by TSI, Inc. The optics system, shown in Figure 4, was used to produce parallel beams of each of the two colors in orthogonal planes. After frequency shifting, these four beams were focused to form a single measurement or "probe" volume at approximately the mid-span position of the airfoil in the test section. Dimensions of the measurement region were approximately 2.9 mm (length) x 0.14 mm (width) producing a sufficient number (usually 16) of interference

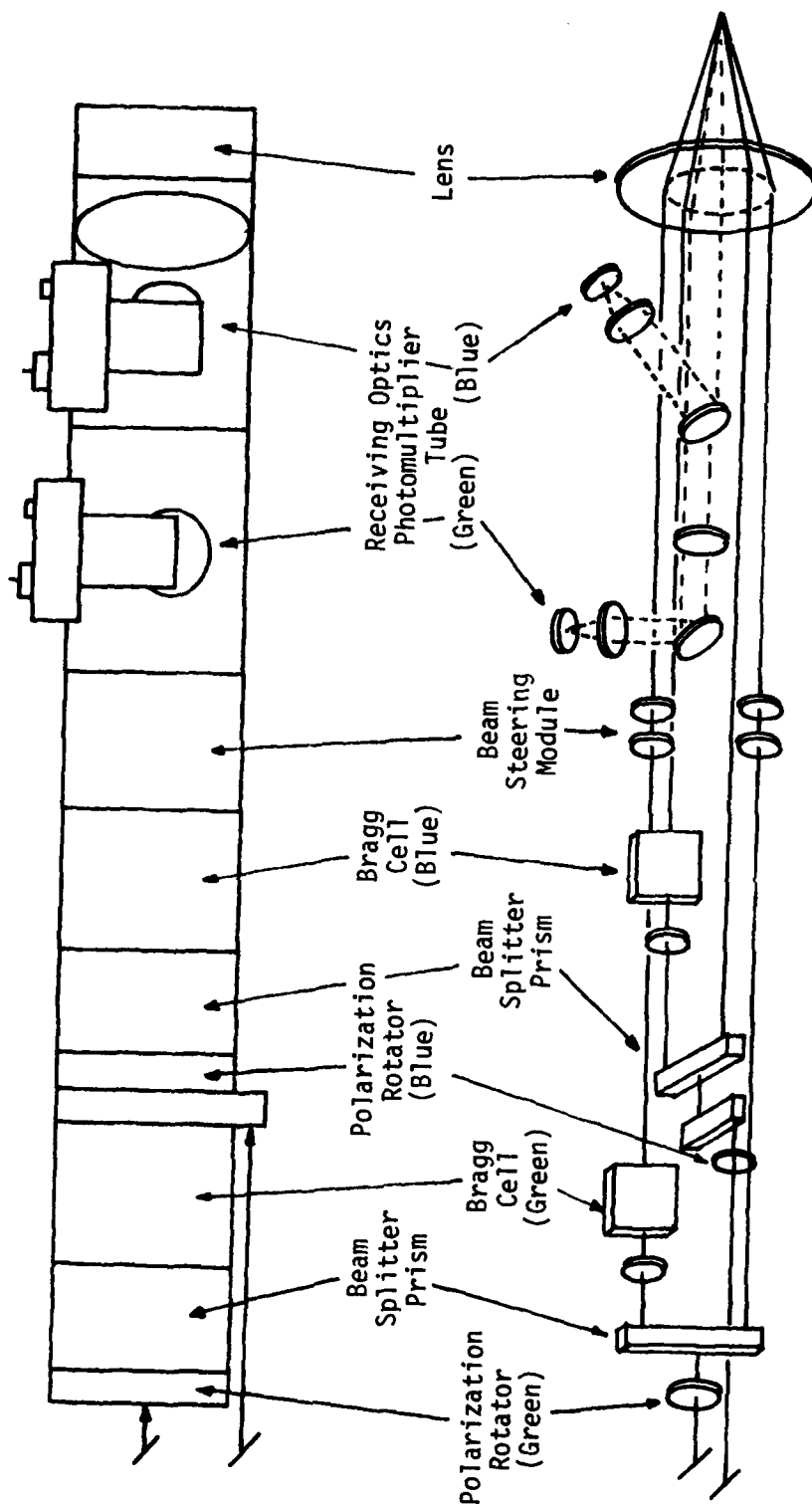


Figure 4. LDV Optical Arrangement

fringe lines. One-half micron (nominal) seeding particles were added to the flow upstream of the test section to produce requisite signal intensities. Backscattered blue and green light was received through collection optics and directed to photomultiplier tubes located in the integrated optics assembly.

Two counter-type electronic processing units (TSI Model 1990) were used to analyze the photomultiplier signals and provide both analog and digital outputs representing the time (or frequency) for a particle to cross a specified number of fringes within the probe volume. The counters also employed an operator-selected data validation scheme which provided for the rejection of spurious signals, thus reducing the data error caused by non-uniform particles or noise. Velocity bias caused by large particles was reduced by a variable threshold control circuit which rejected large amplitude signals. The counters also contained displays to monitor the output data in real time.

A complete sketch of the LDV system configuration is provided in Figure 5. The drive system and optical support structure consisted of a dual axis optical bench truss for orthogonal translation of the probe volume throughout the flow region with relative positioning capability to within 0.025 mm (0.001 inch). The two DC motor drive units were controllable directly from the computer through the digital input/output port interface. A more complete discussion and description of the laser Doppler velocimeter can be found in references 20 and 21.

Among the ambient reference conditions which were continually monitored were the freestream velocity, the tunnel test section temperature, and the ambient pressure.

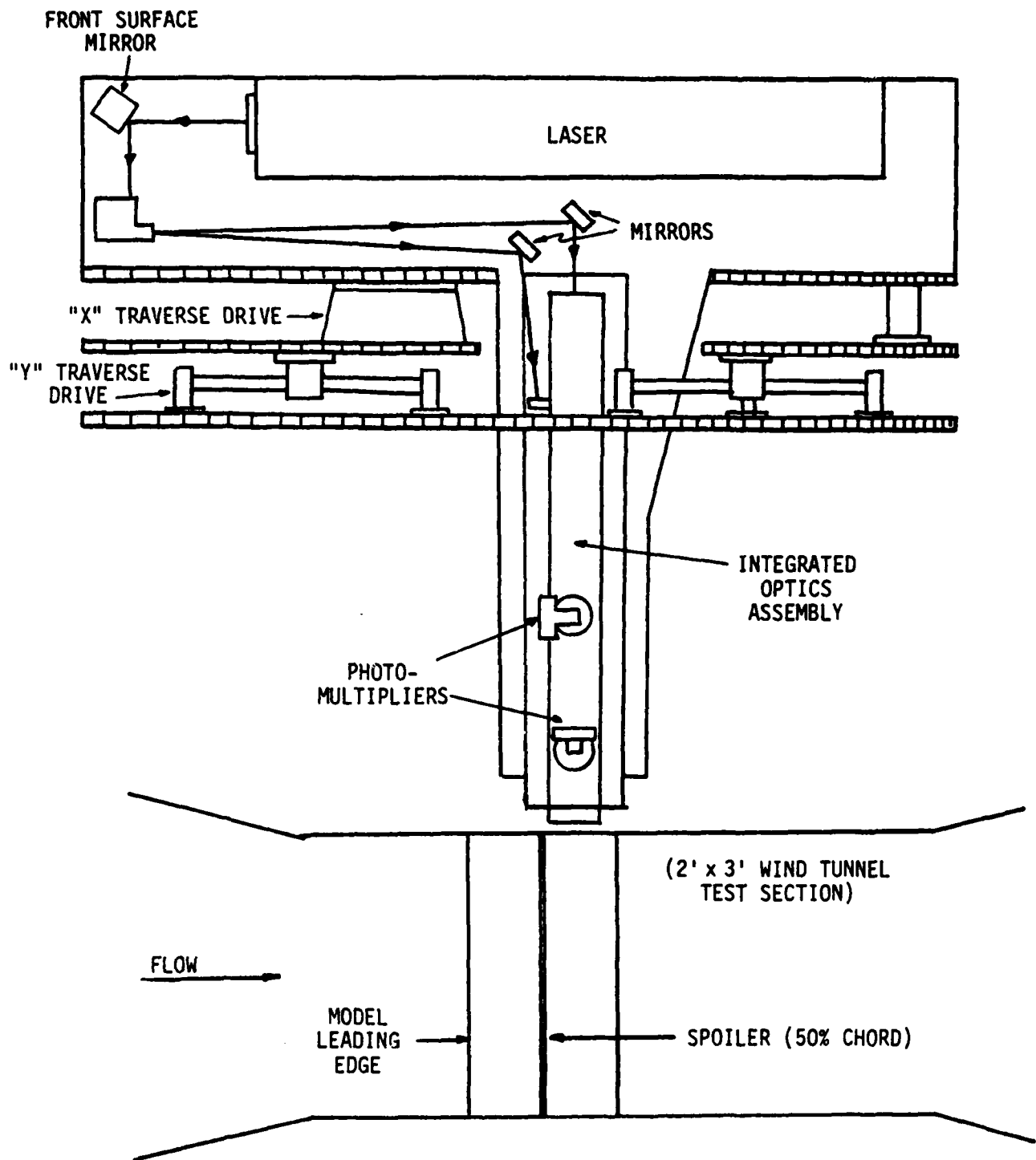


Figure 5. LDV Optical System and Wind Tunnel Test Section

C. Water Tunnel Flow Visualization

Water tunnel experiments were conducted in the U.S. Army Aeromechanics Laboratory water tunnel located at the NASA/Ames Research Center, Moffett Field, California. This facility was selected and employed in part because it provided the capability for exact duplication of the dynamical similarity parameters employed in the wind tunnel experiments. An additional advantage was the ability to achieve low freestream speeds resulting in nominally laminar flow conditions associated with the separated region. Although these extremely low speed results do not correlate with any of the wind tunnel measurements, they provided a useful contrast with high Reynolds number results.

The facility was a closed circuit continuous flow design having a 0.2 m x 0.3 m (8 inch x 12 inch) test section.²² The NACA 0012 airfoil model used in these experiments was geometrically similar to the one described previously but having a 15.2 cm (6 inch) chord. It was constructed from solid aluminum sections, and horizontally spanned the test section. The fence-type spoiler located at mid-chord was capable of sinusoidal oscillation frequencies to 10 Hertz.

The basic technique for flow visualization involved the generation of hydrogen bubbles from surface mounted electrodes through electrolysis. Twelve electrodes of varying lengths and orientation were located along the upper surface of the model. These electrodes consisted of 0.05 mm thick platinum ribbon sandwiched between small sheets of nylon insulating material. The resultant assemblies were embedded in the model using an epoxy filler material so that a single exposed edge served as the active part of each electrode.

The sinusoidal pitching motion of the spoiler was generated through an interface to the oscillation mechanism employed by McAlister and Carr.²³

D. Measurement Conditions

The spoiler geometry parameters used in the wind tunnel measurements were fixed so that the minimum height coincided with the local airfoil surface while the maximum height was maintained at a value of 1.27 cm (0.5 inches).

All measurements were made with the airfoil set to a geometric angle of attack of zero degrees. This provided a suitably thin boundary layer over the surface upstream of the spoiler thereby minimizing any interaction with the separation zone downstream. The freestream velocity ranged from approximately 12.2 meters per second (40 feet per second) to 41.1 meters per second (135 feet per second) in the wind tunnel experiments resulting in a Reynolds number variation of $164,000 \leq R_e \leq 554,000$. This Reynolds number range was expanded during the water tunnel experiments to include reduced values down to 6,000.

EXPERIMENTAL METHODS

A. Averaging Technique

The advantages of employing the vorticity distribution to characterize the flow field were addressed earlier. The extraction of the time-varying mean value of a given flow variable requires a method of generating a phase-locked ensemble average of the signal characterizing the parameter. The sampling of an analog signal from a transducer representing a given variable can be synchronized to a cyclically repeatable event like a prescribed value of the spoiler height. The resultant record representing instantaneous behavior during the subsequent cycle can be stored in the computer memory. Using a prescribed number of these correlated records, the ensemble averages can be generated at select phase points to provide a time history of the mean and statistical variance of the variable at that spatial location.

Using this technique, the generation of averages from the surface pressure transducer and hot-wire anemometer signals was relatively straightforward since continuous analog signals were available. A synchronous sampling scheme initiated by the phase-locked optical trigger circuit was employed with precision limited only by the accuracy of the computer system clock.

Several preliminary experiments were designed to determine a requisite minimum number of records needed for a reliable average to adequately define the mean. Measurements conducted using 1, 5, 25, 50, and 100 record averages revealed that convergence occurred rapidly with an increasing number of records. A 25-record average was selected for use in all measurements of the surface pressure distribution and velocity field as determined with the hot-film anemometer. Even in highly turbulent regions, the net results

were found to deviate from the true mean (as determined by much larger record sizes) by only a few percent.

The measurement of the time varying mean velocity using the laser Doppler velocimeter was not possible using the sampling and averaging scheme described above due to the discontinuous nature of the data signal, i.e., measurement times based on random arrival of signals from seed particles in the measurement volume. As a result, an algorithm (Figure 6) was developed which combined the best features of the synchronous data sampling concept with the irregular digital signals which were obtained in lightly seeded regions using the LDV. Raw data (a digital word representing the magnitude of a velocity component and the acquisition time) was sampled when available and associated with the appropriate temporal "sampling window" according to its phase value. The number of equal width sampling windows defined over the spoiler cycle determined the temporal resolution of the data with respect to spoiler phase.

Sampling was repeated for a total user-specified number of data points whose value was related to factors such as the number of sampling windows per spoiler cycle and the local seeding level. After a prescribed number of samples were acquired, each data word was converted to an appropriate velocity value. At this point additional software corrections directed at the reduction of measurement errors were also employed. Continuous sampling prior to data word conversion and subsequent redistribution into a data array was accomplished to maximize the acquisition throughput rate and, therefore, minimize the number of lost valid data words which may have occurred during the execution of data processing software commands.

Each data value was then added to a location in a "data accumulator" array. The corresponding window in the sample number accumulator array

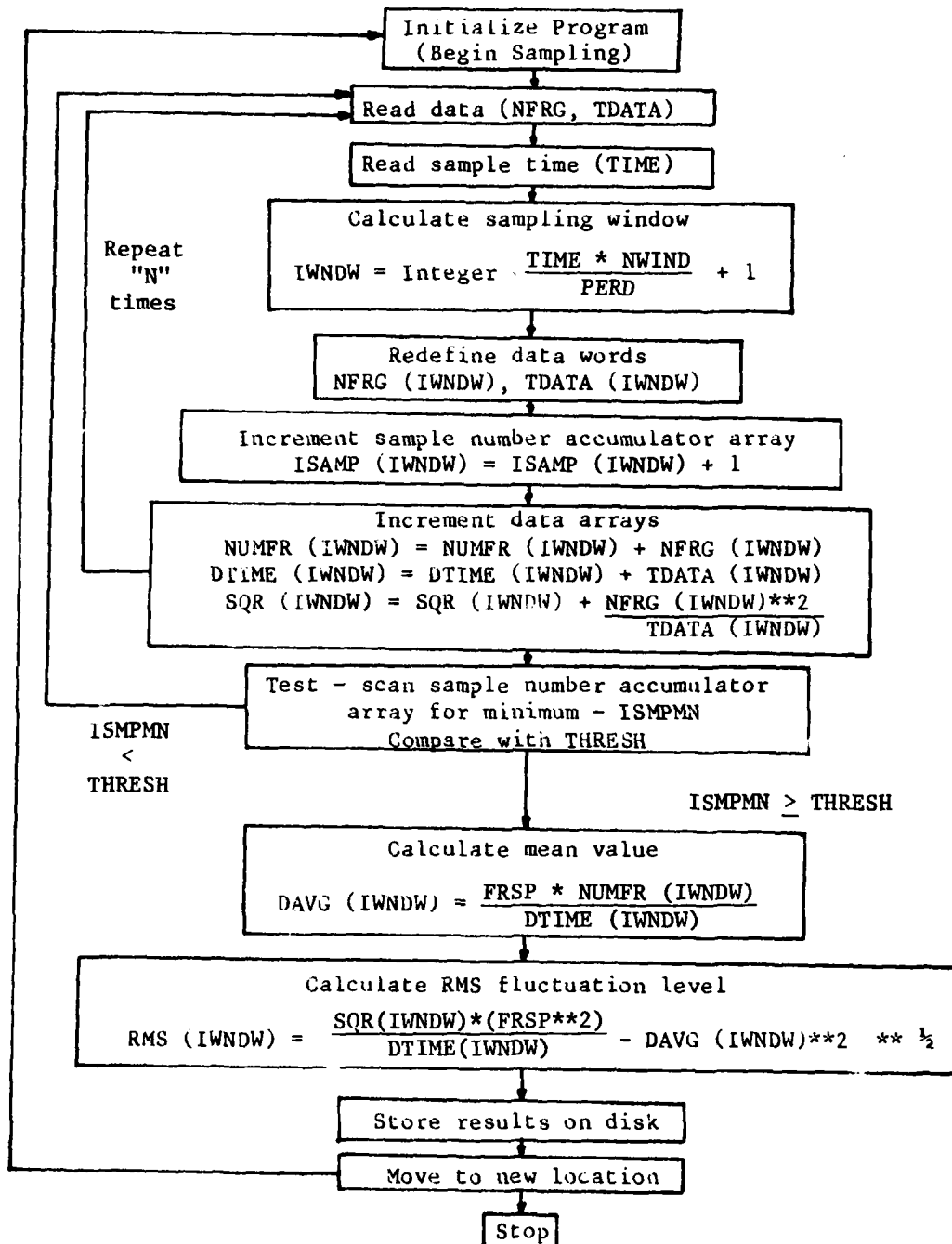
Program Initialization

1. Select data channel (incorporates correct wavelength data)
2. Record measurement location
3. Select and record motion period, PERD (defines length of record)
4. Select sampling threshold (ITHRESH)
5. Select consecutive sample loop size (N)
6. Select number of windows defining motion cycle (NWIND)
7. Define array/buffer sizes (depends on processor/computer)
8. Reset clock (automatic with start of each new cycle)

Definition of Variables

1. IWNDW - integer representing width of measurement window
2. NFRG - number of fringes traversed during a 'burst' (fixed or variable)
3. TDATA - time to traverse NFRG fringes during a given burst
4. TIME - sample time

Figure 6(a). Algorithm Incorporating Total Velocity Vector (Residence Time) Bias Correction



NFRG is fixed constant in the 'N'-cycle mode

Figure 6(a) (cont). Algorithm Incorporating Total Velocity Vector (Residence Time) Bias Correction

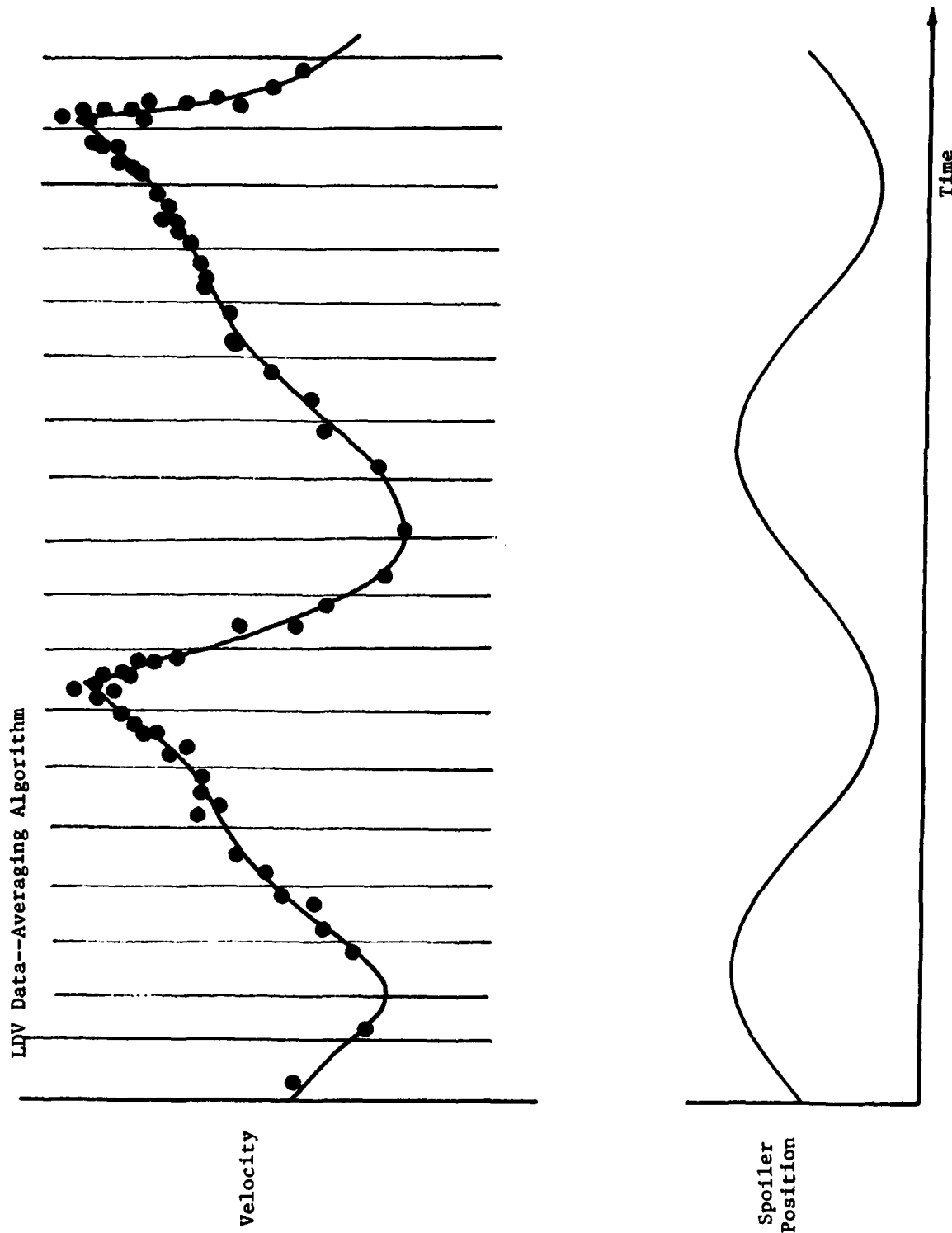


Figure 6(b). Algorithm Incorporating Total Velocity Vector (Residence Time) Bias Correction

(indicating the number of valid data words accumulated at each phase point) was then incremented. The assignment of information to these two storage locations was controlled by the value of the sampling time parameter. When a predetermined value was reached in the "worst case" sampling window in the sample number accumulator array, the measurement at that spatial location was terminated. Averaging for each sampling window was based on the corresponding value in the sample number accumulator array (total data points). Additional details related to the implementation of this technique including the incorporation of velocity and fringe bias corrections are contained in reference 21.

B. Vorticity Measurement Technique

The vorticity field was inferred from velocity field measurements using a technique described previously by Francis, et. al.,²⁴ and extended to unsteady flows by Keese, et. al.²⁵ The technique involves the literal application of the definition of circulation, i.e., the integration of the appropriate velocity component around a closed contour.

$$\Gamma(t) = \oint_C \vec{u}(\vec{x}, t) \cdot d\vec{x} \quad (2)$$

If the contour is chosen to lie in the x-y plane, for example, and A is the resulting enclosed planar area, the expression for the spatially averaged component of vorticity orthogonal to the measurement plane can be expressed as

$$\langle \xi_z(t) \rangle = \frac{1}{A} \oint_C \vec{u}(x, y, t) \cdot d\vec{x} \quad (3)$$

If a number of small contours are arranged in an aggregate, the distribution of vorticity in the enclosed region can be inferred. Since equation

(3) is the result of kinematic conditions, a contour, C , may take any shape. In practice it is convenient to choose a contour array geometry which is related to the flow being investigated or the experimental apparatus being employed. Selection of this geometry in the present case was based on a number of factors including the probe measurement volume, the location and size of the separated region and shear layer, and the desired resolution of the vorticity field. The time varying mean value of the vorticity for the "i"-th element of the mesh is given by

$$\langle \xi_z(t) \rangle_i = \frac{1}{A_i} \oint_C \overline{\vec{u}(\vec{x}, t)} \cdot d\vec{x} \quad (4)$$

A schematic of the rectangular mesh which was used in the present case is provided in Figure 7. In this case a total of 390 sampling locations was employed. The choice of this configuration was predicated on the knowledge of the flow field obtained from flow visualization information.

The data reduction algorithm involved the conversion of hot-film signal voltage data to velocity, appropriate testing for data validity including flow angle and magnitude determination, ensemble averaging, and subsequent storage of the averaged data on disk.²⁵ Each data set was tagged with the probe location and aerodynamic reference data (pressure, temperature, free-stream velocity, etc.). Upon completion of the storage of each data set, program control was exercised to reposition the probe through the digital-to-analog converter voltage output. The repositioning and acquisition sequence was repeated through the entire array of spatial locations. Upon completion of the measurements, the spoiler was retracted and the reference variables remeasured to calculate the total drift in the electronics system and the ambient freestream conditions. Drift problems posed a major source

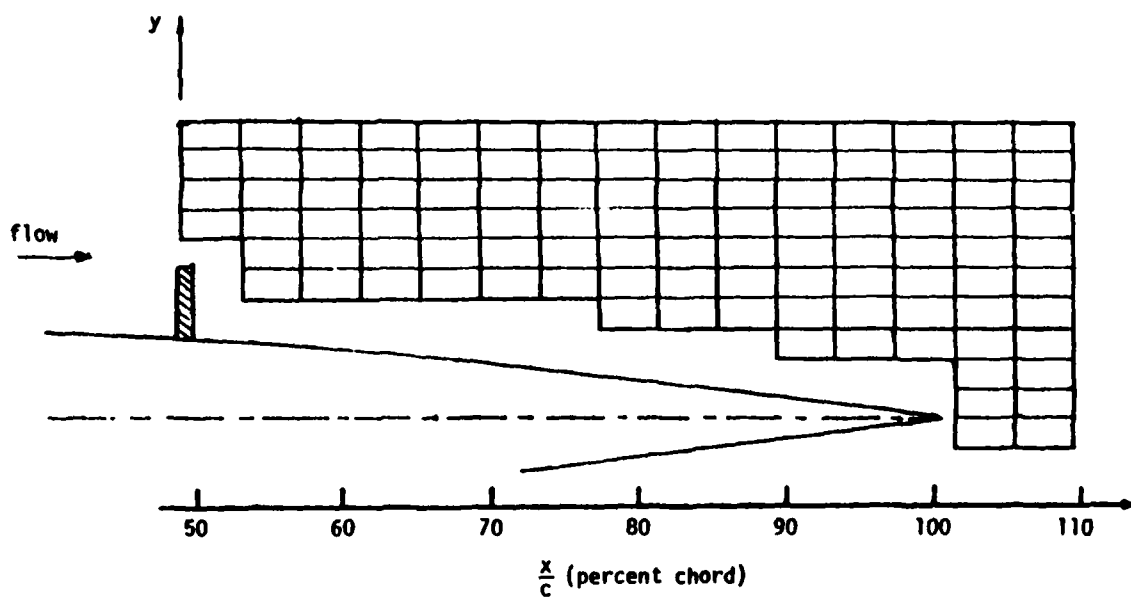


Figure 7. Contour Array Geometry - Outer Shear Layer

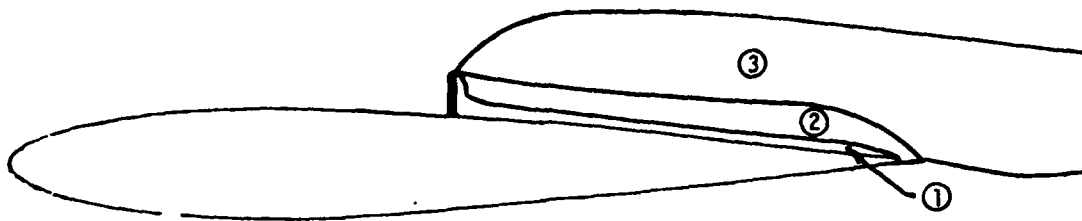
of possible error due to the extensive measurement time intervals encountered. The total time involved in the completion of a typical experiment varied from approximately 42 minutes at high spoiler frequencies to a maximum of about 4.5 hours at the lowest frequencies. This problem can be more fully appreciated by realizing that while only 72,000 data words were actually stored during a typical experiment, approximately 1.8×10^6 data words were acquired and processed by the computer during the same period. (Instantaneous velocity records were not stored on disk.)

Upon completion of the experiment, disk-stored average data were recalled to core memory for the spatial integration calculations. Data from select measurement points were integrated to provide the circulation of various mesh elements at discrete phase points. Repetition of the integration procedure for the other phase angles then provided the entire spatial and temporal distributions.

C. Sources of Error

The use of miniature dynamic piezoresistive transducers to assess the surface pressure distribution was straightforward and has been documented previously.¹⁸ The nature of errors incurred in the application of the vorticity measurement technique to an unsteady separated flow, however, is not immediately apparent.

The use of the hot-film anemometer presented certain limitations on the possible measurement locations due to the intermittent, reversing nature of the flow. Flow reversal was found to be the most pronounced near the airfoil surface with a low velocity region existing immediately behind the spoiler and extending downstream (Figure 8). The use of the hot-film technique was therefore confined to the outer shear layer region and a portion



- 1 - Strong flow reversal over large portion of cycle-measurements unreliable.
- 2 - Some flow reversal during parts of the cycle-measurements marginally reliable.
- 3 - Outer shear layer-measurements valid over most of cycle.

Figure 8. Flow Regions During Separation Process

of the "dead air zone." To further insure that only valid data were sampled, the values of several additional variables were monitored to insure that erroneous data were not collected. Data locations where the local x-component of velocity did not exceed 25% of the freestream value were annotated. In addition, a computation of the root mean square values of both the u and v velocity components was obtained at select sampling locations. Signals were continuously monitored for overrange conditions. Values of the instantaneous "X"-wire crossflow angle were also computed to insure that the flow angle was maintained within the linear limits of operation ($-0.5 < \tan \delta < +0.5$). Results from a survey of this variable over the entire extent of the measurement array has shown that the flow angle never exceeded the linear limit of validity for more than 1.4% of the total measurement time, in the worst case. A more complete discussion of the limitations of applying the "X"-configuration probe to this type of measurement, especially with regard to the out-of-planeness velocity component error, is provided in reference 24.

Other sources of measurement error include probe positioning resolution, sampling accuracy, and the accuracy of the spatial integration scheme.²⁵ A worst case value for the total error for a typical contour employed in the present experiment has been estimated at approximately 2.5%.

EXPERIMENTAL RESULTS

A. Steady Flow Description

Although the primary intent of this report is to describe the global effects resulting from forced spoiler oscillations, it is useful to briefly discuss the flow character with fixed spoiler height. With the spoiler fully retracted (flush with the airfoil surface) and low Reynolds number freestream conditions, a thickened boundary layer on the airfoil surface was observed to evolve into a trailing edge separation condition. Periodically shed vortices, similar to those associated with the classic Karman vortex street, were detected in the near wake region. The separation zone adjacent to the airfoil surface near the trailing edge was characterized by a low energy eddy bounded by a laminar shear layer (the separated boundary layer). An increase in the freestream velocity resulted in rearward movement of the separation point and a thinning of the upstream boundary layer.²⁶ The frequency of the shed vortices was observed to increase while the characteristic size decreased. Also, organized, discreet shedding was observed to evolve to a turbulent random nature with a sufficient increase in Reynolds number.

An extension of the spoiler to even a small distance resulted in detectable separation at the spoiler. Increasing the spoiler height resulted in the perceptible increase of the length of the separated region. With the spoiler fully extended, reattachment or, more properly, confluence was observed to occur well into the wake region. An increase in the Reynolds number under these conditions had the effect of increasing the mixing in the shear layer between the separation zone and the outer potential flow. In addition, the mean rotational velocity of the separation eddy was also observed to increase with Reynolds number.

It is also useful to describe the mean vorticity field associated with the shear layer behind the spoiler. A representative contour integral map of this variable is presented in Figure 9 for the case where the spoiler is extended to its maximum height above the surface. The contours are presented for appropriately nondimensionalized values of the vorticity as follows:

$$\xi_z' = \frac{\xi_z c}{2U_\infty} \quad (5)$$

This variable is similar in structure to the dimensionless frequency (k) giving it the same form as the Strouhal number.

Upon examination of Figure 9, the symmetry of the shear layer with respect to the freestream direction about a line extending downstream from the tip of the spoiler is apparent. Although this figure shows the result for only a single value of the freestream Reynolds number, similar results occurred over the entire range of Reynolds numbers examined. Not only were the shear layer characteristics symmetrical in these cases as well, but the contour lines representing identical values of the dimensionless vorticity were observed to almost coincide with the same spatial locations. This comparison suggests that the dimensionless vorticity expressed in the form presented above represents a similarity variable, at least in the steady flow case. Additionally, this implies that the local strength of the vorticity field is proportional to the freestream velocity.

Previous investigators have noted that the length of the separated region based on the reattachment point appears to vary linearly with the value of the spoiler height in steady flow. This is similar to the result obtained for a turbulent mixing layer in which the shear layer thickness is observed to vary linearly with the downstream coordinate variable.²⁷ For

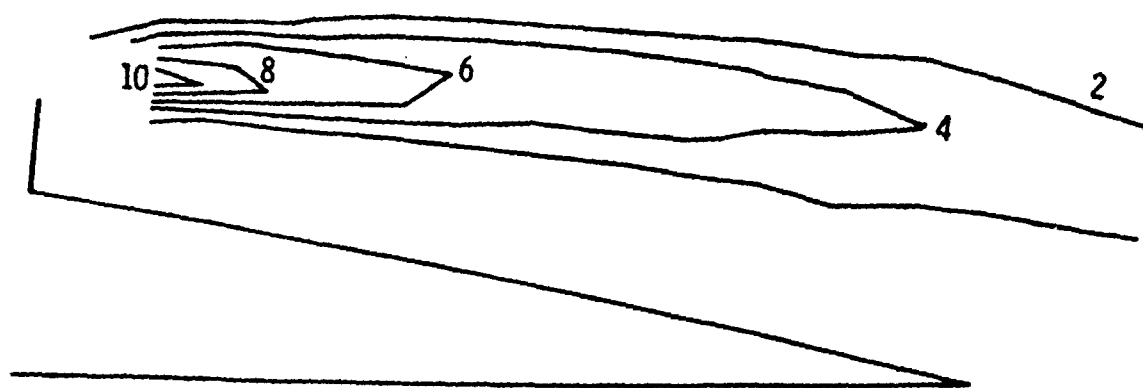


Figure 9. Iso-vorticity Contours Associated with Steady Flow Separation, Spoiler Fully Extended, $Re = 287,000$ ($U_{\infty} = 70$ ft/sec)

a given value of spoiler height, the location at which the shear layer's lower boundary intercepts the airfoil surface, l , can be expressed as

$$l = K_1 h_s \quad (6)$$

where K_1 is a constant. One concludes, therefore, that the existence of a nearly symmetrical shear layer is consistent with previous models of separation which portray it as a "bubble"-like structure whose geometry is linked directly to the spoiler height. It is, therefore, not surprising that early attempts to characterize the separation zone generated through unsteady motion of the spoiler involved merely a modification to the "bubble" concept to include a characteristic phase lag associated with the frequency of the unsteady motion.¹⁸

It must be emphasized that these results are applicable for the case of maximum spoiler extension. The expected linear relationship between spoiler height and separated region length will only occur if the spoiler extension distance is sufficiently greater than the normal thickness of the upstream boundary layer so that its effect is that of an overwhelming disturbance when compared to the boundary layer geometry.

B. Effects of Spoiler Oscillation at Low Reynolds Numbers

When the spoiler was oscillated in simple harmonic motion, even at very low frequencies, unsteady effects were evident. The resultant separation at low Reynolds numbers appeared to be laminar in character with an almost cylindrically symmetric rolled-up vortex sheet originating at the spoiler and convecting along the airfoil surface.²⁶

Results from a typical cycle of oscillation for these conditions are presented in Figure 10. This series of photographs graphically depicts the formation and movement of the primary vortex structure. Not so apparent is



(a) $\phi = 0^\circ$



(d) $\phi = 180^\circ$



(b) $\phi = 60^\circ$



(e) $\phi = 240^\circ$



(c) $\phi = 120^\circ$



(f) $\phi = 300^\circ$

Figure 10. Unsteady Separation at Low Reynolds Number,
 $k = 3.70$, $Re = 10,000$

the extremely energetic flow reversal which occurs during the initial stages of vortex formation during the spoiler upstroke. A backflow into the region immediately behind the spoiler and up along the aft face of the spoiler is redirected rearward at the spoiler tip along with fluid emanating from the upstream region. A vortex-like structure results which appears to move almost as a solid body along the airfoil surface at a fraction of the free-stream speed.

The number of vortex structures which can exist over the surface of the airfoil at any given time is primarily a function of dimensionless frequency. As the frequency is increased, one observes a longer effective residence time in terms of the spoiler oscillation, thereby allowing more vortices to exist on the airfoil at any given time.

Also apparent at these low Reynolds numbers is the presence of secondary vortex-like structures which are formed nearer the trailing edge due to roll-up of the shear layer. They are not generated directly by spoiler motion but appear related to a spoiler induced shear layer instability. Their character is a strong function of both Reynolds number and dimensionless frequency,²⁶ and they can apparently interact strongly with the primary vortex depending on their relative location and the flow conditions during generation. Using high speed motion pictures, one might either observe the primary vortex ingest the secondary structure, or an interaction which culminates in the rapid breakup of both structures through turbulence.

All of the low Reynolds number flow visualization data were obtained at high values of dimensionless frequency, and these measurements strongly support the notion that unsteady separation does not generally involve a growing and shrinking bubble as previously conceptualized, but may more properly be characterized by a coherent vorticity-bearing region which can

grow, diffuse, and eventually convect into the airfoil wake region while simultaneously affecting local surface loading in a significant fashion.

C. Unsteady Flow at High Reynolds Numbers

Visualization of higher Reynolds number flows does not reveal as coherent a structure as that observed in a laminar, low speed case due to the high levels of turbulence. One does, however, observe a qualitatively similar growth progression involving an energetic flow reversal followed by an observable rotating, eddy-like structure.

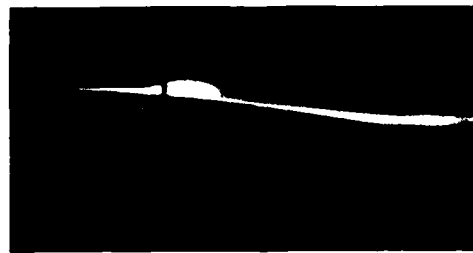
An example of hydrogen bubble flow visualization for these flows can be found in Figure 11. In viewing these results, the geometric characteristics of the separation zone are measurable despite the detrimental effects of turbulent mixing on the quality of visualization. Mixing between the potential flow region and the circulating region behind the spoiler appears to be quite strong in the outer shear layer interface. Reattachment is observed initially to occur on the airfoil surface during initial stages of the spoiler upstroke, but extends into the wake region during midcycle and on the downstroke. Even in these high Reynolds number cases, the nature of the separated region does not fully resemble a "bubble" which grows and contracts as previously thought. A more complete discussion of flow visualization experiments at higher Reynolds numbers can be found in Reference 26.

D. Unsteady Vorticity Field in the Outer Shear Layer

The vorticity field associated with a fixed extension of the spoiler can be contrasted with a flow field behavior evoked by unsteady spoiler oscillations. Outer shear layer flow field development obtained through hot-film anemometer measurements is displayed for an average cycle of motion for two different values of the dimensionless frequency in Figures 12 and



(a) $\phi = 0^\circ$



(d) $\phi = 90^\circ$



(b) $\phi = 30^\circ$



(e) $\phi = 120^\circ$



(c) $\phi = 60^\circ$

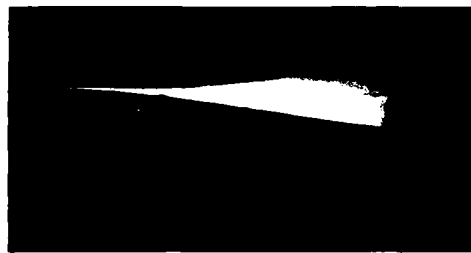


(f) $\phi = 150^\circ$

Figure 11. Unsteady Separation at High Reynolds Number,
 $k = 0.85$, $Re = 246,000$



(g) $\phi = 180^\circ$



(j) $\phi = 270^\circ$



(h) $\phi = 210^\circ$



(k) $\phi = 300^\circ$



(i) $\phi = 240^\circ$



(l) $\phi = 330^\circ$

Figure 11 (cont). Unsteady Separation at High Reynolds
Number, $k = 0.85$, $Re = 246,000$

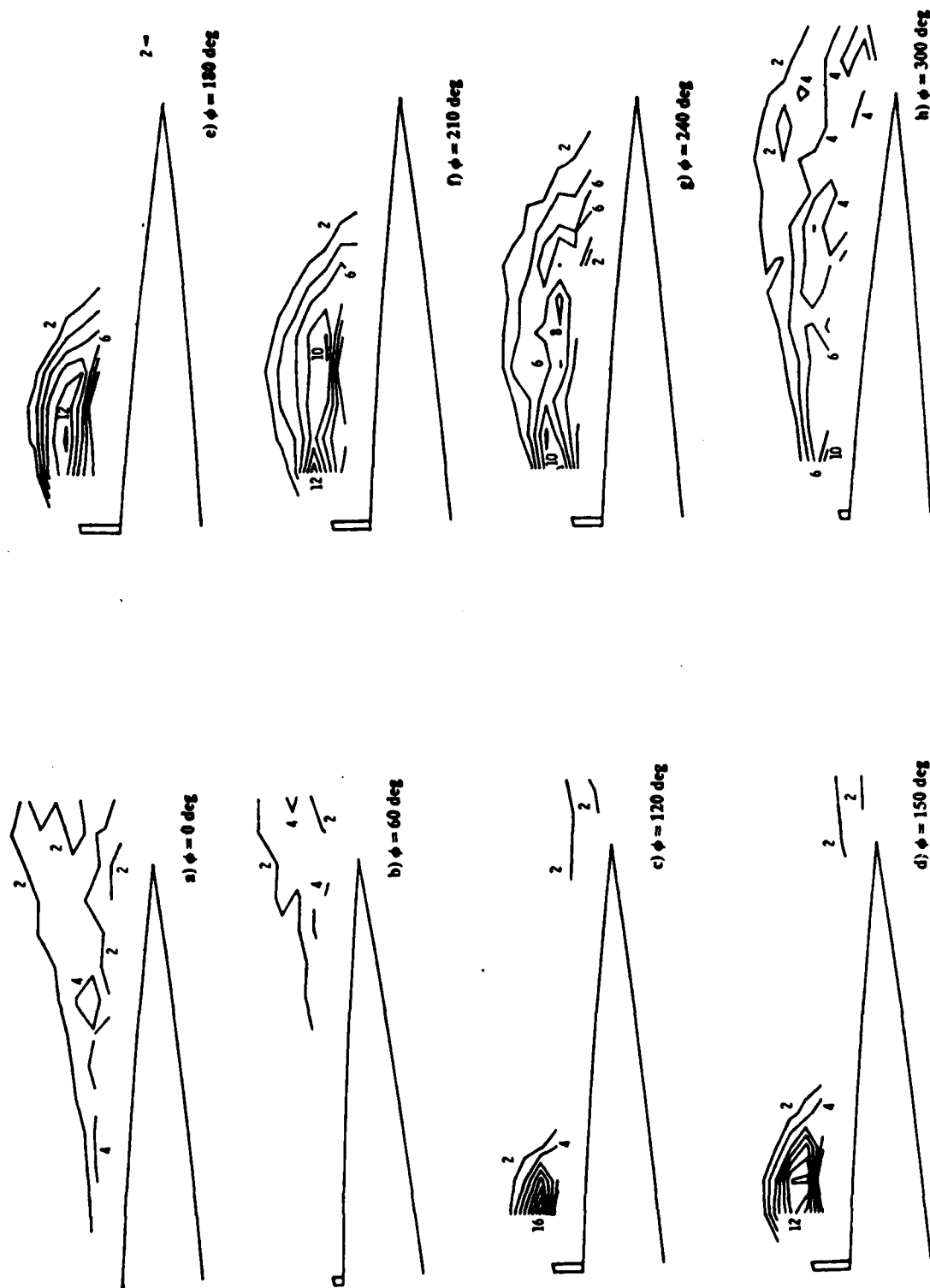


Figure 12. Iso-vorticity contours associated with unsteady flow separation,
 $k = 1.2$, $Re = 180,000$ ($U_\infty = 60 \text{ ft/sec}$)

13. The evolution of the unsteady separation zone is shown using contour maps at equally spaced values of the phase angle.

An examination of the upstroke portion of the cycle in Figure 12 reveals the formation and growth of an energetic vortex-like structure downstream of the spoiler. This interpretation is confirmed by the high level of vorticity observed and the high degree of curvature in the shear layer geometry when compared to steady flow results. A similar vortex is observed in the low frequency example (Figure 13) but with less curvature in the shear layer shape sustained for a shorter portion of the cycle. While the growth lag described by previous investigators is apparent, the characterization of the separation zone interior as a "dead-air region" must be questioned, at least during the early part of the cycle. The higher peak vorticity magnitudes observed in the unsteady cases come as no surprise when one considers that there are now two sources of vorticity, one being the action of the freestream as it passes over the spoiler tip and the other related to the shearing action parallel to the oscillating spoiler face. The energetic, rotating flow is formed by a combination of the fluid motion induced by the spoiler oscillations and the entrainment tendencies of the shear layer generated by the freestream. If one attempts to compare the capability to generate vorticity by these two mechanisms through a ratio of maximum spoiler oscillation velocity to freestream velocity, the resulting parameter is expressed as

$$k' = \left(\frac{h_{s_{\max}}}{c} \right) k \quad (7)$$

As the value of this modified, dimensionless frequency parameter approaches unity, one expects that the capability for vorticity generation from these two mechanisms becomes comparable.

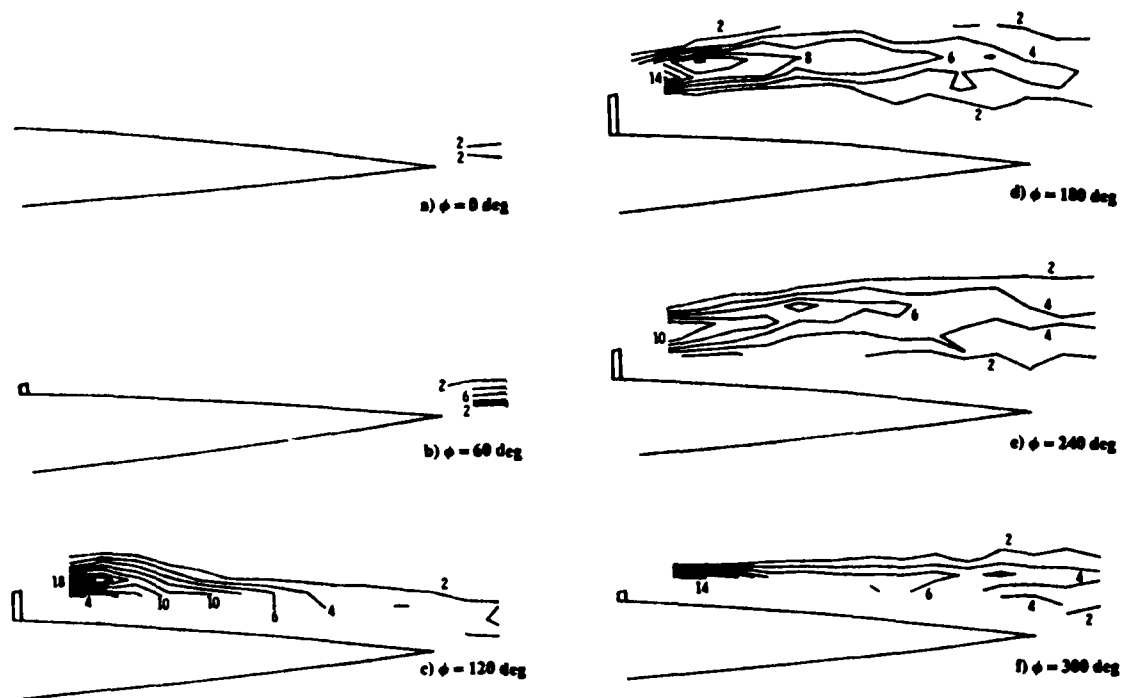


Figure 13. Iso-vorticity Contours Associated with Unsteady Flow Separation, $k = 0.2$, $Re = 287,000$ ($U_\infty = 70$ ft/sec)

The structure of the tightly wound vortex is observed to deform significantly under the influence of the freestream during the mid-portion of the cycle. As the spoiler nears its maximum height, its velocity, \dot{h}_s , slows rapidly. The result at low frequencies is that the flow field attempts to "catch up" with the corresponding steady flow configuration (see Figure 9). At dimensionless frequencies near unity, the downstroke portion of the cycle is observed to begin before this relaxation of the shear layer can occur. As a result, a flow configuration resembling that encountered in steady flow never really develops.

As the separation zone expands in time, lower peak amplitudes of vorticity are observed due to the action of viscosity and flow turbulence as well as through convection by the freestream. Except for that time segment during which vortex formation is prevalent (on the upstroke), maximum vorticity levels occur near the spoiler tip and are caused by the action of the accelerated freestream in that area.

While the growth of the separated region on the spoiler upstroke might be viewed loosely as a "bubble"-like structure whose characteristic size lags a corresponding steady flow value, no such interpretation can result from an observation of the vorticity field on the spoiler downstroke. At low frequency, the detached shear layer appears to retract toward the airfoil surface with the spoiler in a quasi-steady manner. At higher frequencies, however, the vorticity bearing structure is observed to completely detach from the spoiler and convect off the surface.

The deformation of the tightly wound vortex through entrainment by the freestream-generated shear layer prompts an inquiry regarding the conditions for which this structure might be capable of sustaining its cylindrical symmetry throughout the motion cycle. The ability of the vortex to retain

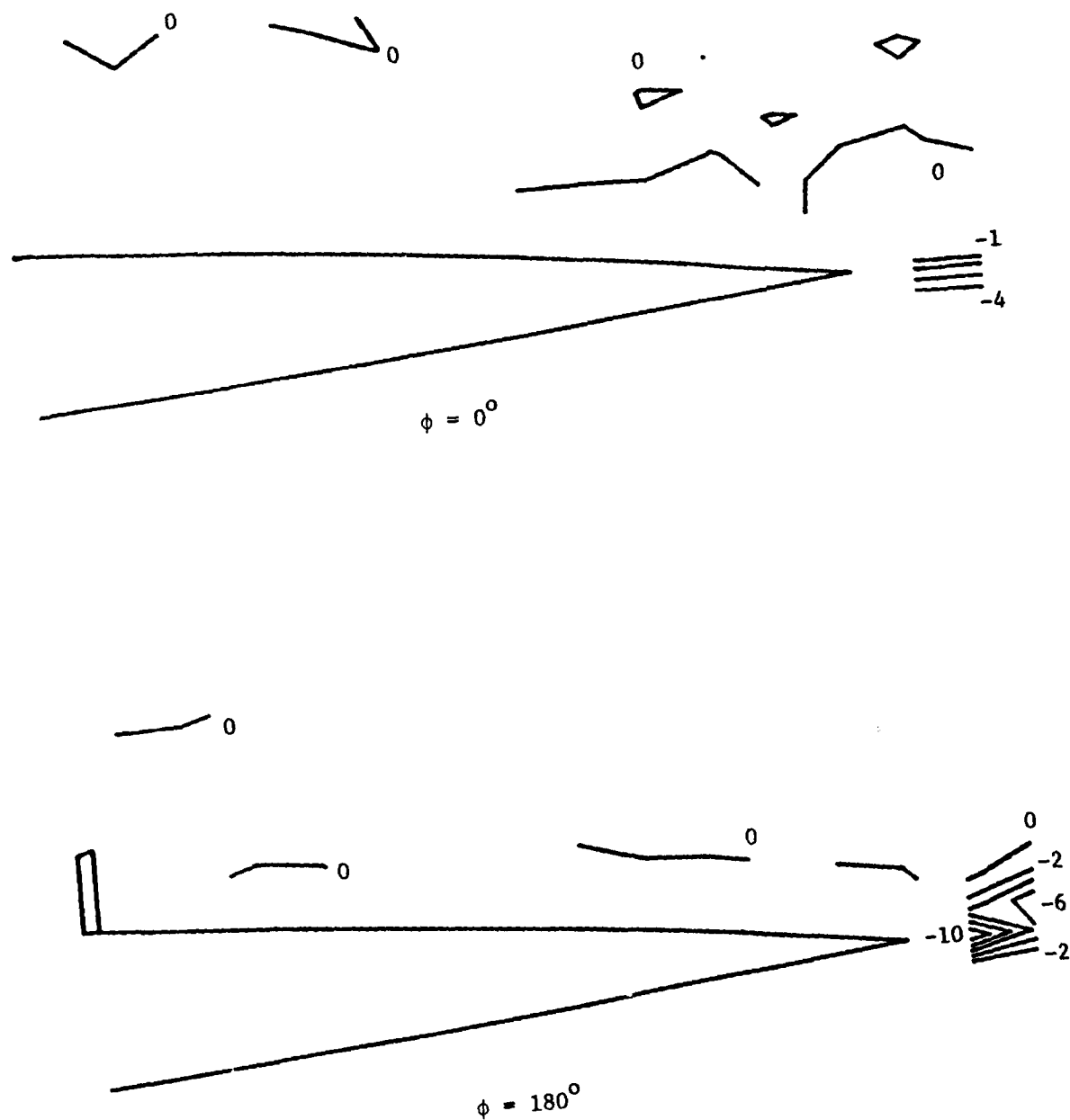
its identity in this case would seem to somehow depend on the ratio of the energy of the rotational motion associated with the vortex as compared to the freestream kinetic energy. Simple dimensional arguments show that this ratio is proportional to the square of the dimensionless frequency. As the value of this ratio approaches unity, the vortex might then be able to maintain its structure at least through its traversal over the upper surface of the airfoil.

It should be emphasized that the effects of turbulence have not been accounted for in this simple argument, and these also must be taken into consideration when attempting to develop a more accurate characterization of separated region development at high Reynolds numbers.

Thus far, all discussion has centered around vorticity directed in the positive z-direction (sense into the page) which is generated primarily during the upstroke. Vorticity of the opposite sign is also observed in the measurement region, the most significant quantities being found in the wake downstream of the airfoil trailing edge during the latter part of the downstroke. This opposite-signed vorticity appears to be generated on the lower airfoil surface and is believed to be a response to rapid changes in the circulation associated with the separated region in an attempt to satisfy the Kutta condition at the trailing edge (Figure 14).

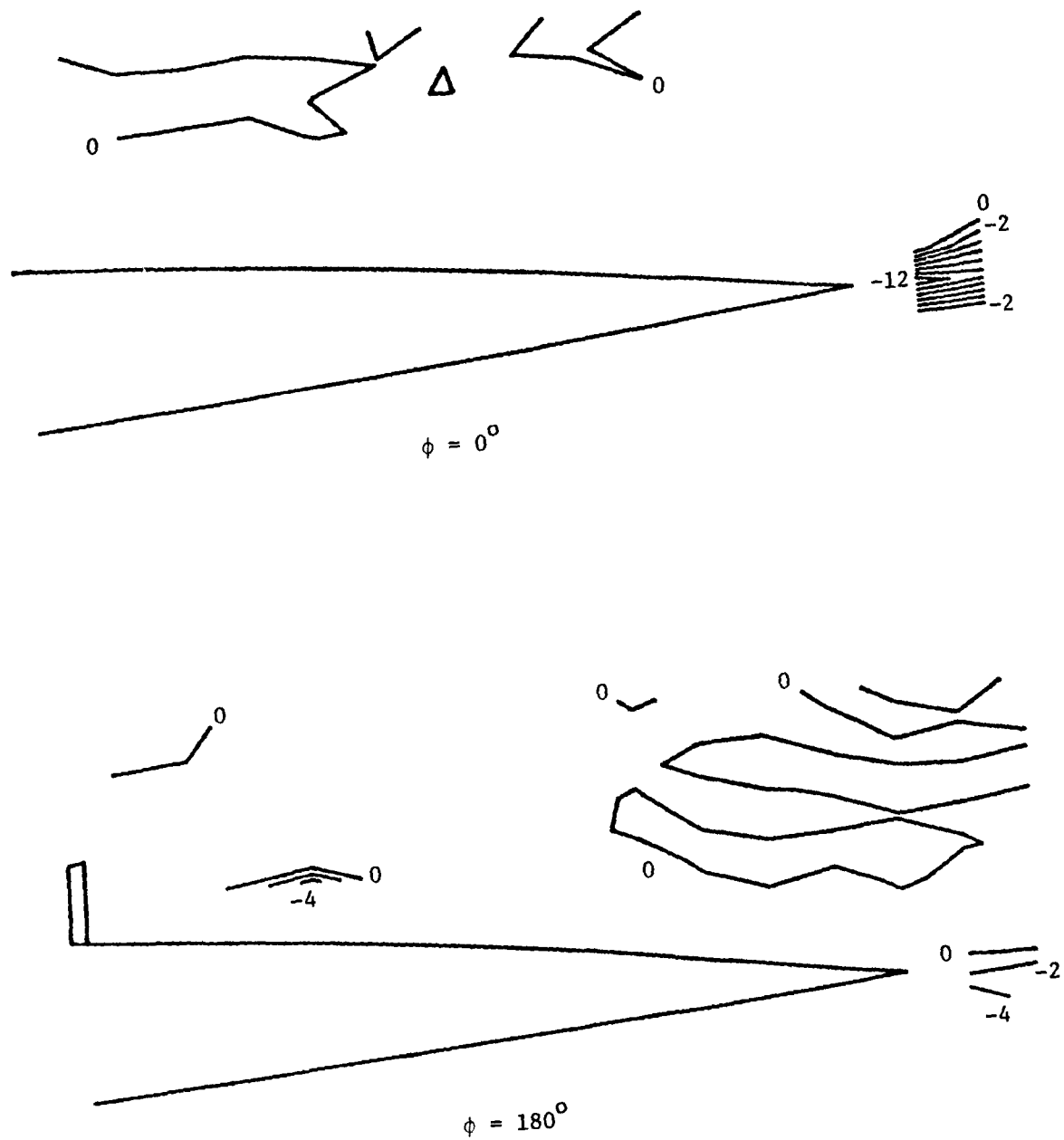
E. Vortex Growth Characteristics

Of particular interest in the evolution of the unsteady separated flow field are the detailed growth characteristics of the structure formed behind the spoiler during the upstroke motion. The development of the vortex geometry is of significance if one accepts the premise that vortex induced velocities near the surface are responsible for the significant suction levels discussed in the next section.



(a) $k = 0.20$, $Re = 287,000$

Figure 14. Iso-Vorticity Contours in the Outer Shear Layer - Negative Vorticity



(b) $k = 1.2$, $Re = 180,000$

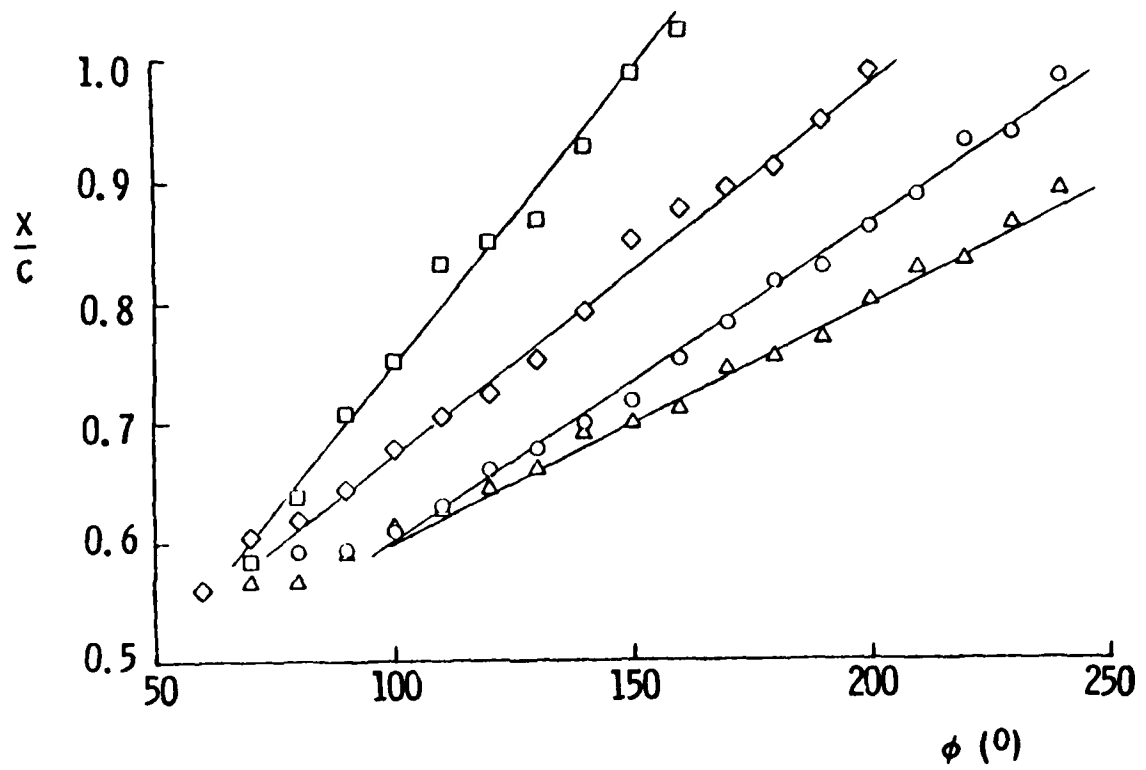
Figure 14 (cont.). Iso-Vorticity Contours in the Outer Shear Layer - Negative Vorticity

Initial detection of the vortex using the hot-film anemometer did not occur until the phase angle reached a value of approximately 40-70 degrees and when the characteristic dimensions of the structure were of the order of h_{smax} .

The combined decrease of maximum rotation rates with chordwise elongation and lateral expansion made it exceedingly difficult to formulate a single parameter capable of relating all facets of vortex growth. As a result, each of these characteristic traits related to vortex evolution will be dealt with individually.

The lateral extent of the outer shear layer appeared to be controlled primarily by the value of the spoiler height. The longitudinal growth of the vortex, however, was found to be related primarily to the oscillation frequency. The measurement of the length of the separation zone was accomplished by tracking the motion of the individual iso-vorticity contours in the x-direction at prescribed values of the lateral (y) coordinate. Some of these results are presented in Figure 15 for several combinations of dimensionless frequency and Reynolds number. The nearly linear nature of these characteristics suggests that the growth of the vortex is directly proportional to the time of evolution (phase angle) and not correlated to the non-linear motion of the spoiler itself, at least during the mid-portion of the upstroke. One observes that the higher the value of k , the more extensive is the linear region. An alternative statement is that the vortex remains as an identifiable entity for a larger fraction of the period at higher frequencies.

The individual slopes of the lines shown in this figure can be used to provide the values of the characteristic longitudinal growth velocity. This variable can be formulated in a dimensionless way as follows:



	$Re \times 10^{-5}$	k
Δ	1.80	1.2
○	2.46	0.85
□	2.87	0.2
◇	2.87	0.5

Figure 15. Length of the Separated Region as a Function of Phase Angle

$$\frac{U_c}{U_\infty} = A \cdot \frac{\Delta(x/c)}{\Delta\phi} \quad (8)$$

where A is an appropriate nondimensionlization factor which can be a function of the dimensionless frequency. Computed values of this parameter from experimental data show that it is not sensitive to freestream Reynolds number, at least over the range examined. A graph of the dimensionless convective velocity variation with the square root of the dimensionless spoiler oscillation frequency is provided in Figure 16. The apparent linear relationship suggested by this result can be expressed as:

$$\frac{U_c}{U_\infty} = B \sqrt{k} \quad (9)$$

where B is a constant probably related to the spoiler mean height and amplitude parameters and which equals 0.28 in the present case. This is an interesting result and one, heretofore, unexplained by any existing theories. One must be cautioned not to confuse the growth parameters of the spoiler-attached vortex discussed here with those of the detached structure formed at high frequencies and much lower Reynolds numbers alluded to previously. Other methods of correlating the vortex growth parameters meet with less success.

The one parameter which appears to correlate closely with Reynolds number is the maximum level of vorticity observed in the different experiments. This was observed for the steady flow examples presented earlier but also appears true in the unsteady flow case. One must be cautious when attempting to draw conclusions from observations of $\xi_{z_{max}}$, especially because of the limited extent of the measurement grid geometry. For this reason, it was felt that a more appropriate parameter might be generated by spatially averaging the vorticity in the y-coordinate direction at various

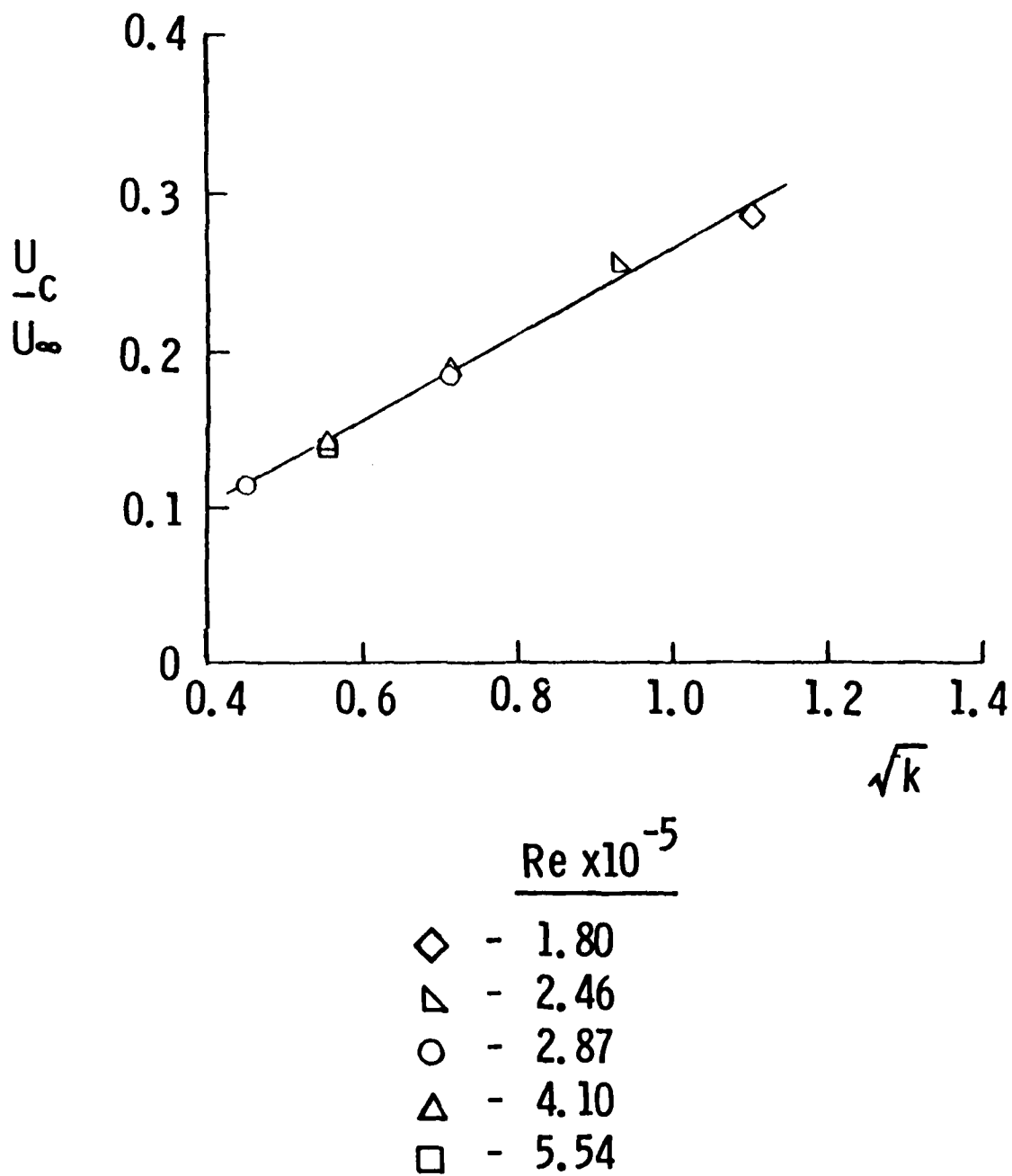


Figure 16. Characteristic Vortex Growth Velocity - Frequency Variation

stations in the downstream direction. The relationship between the maximum value of this laterally-averaged variable detected during a cycle of motion and the Reynolds number is presented in Figure 17. The linear result suggests that the peak levels of vorticity are strongly correlated to the freestream velocity and, therefore, the corresponding Reynolds number.

F. Vorticity Field Correlation with Surface Pressure Field

As stated earlier, an extensive amount of data has been compiled by previous authors concerning the behavior of the surface pressure distribution as it relates to the unsteady separated region.¹⁶⁻¹⁸ In steady flow, an examination of the pressure coefficient downstream of a fixed spoiler protuberance indicates a "roof-top" shape to the pressure distribution. In the case of unsteady spoiler oscillations, this distribution is modified by an increased intensity in the suction peak which is related to the frequency of oscillation as well as a characteristic lag in the growth of the separation zone. These results have been verified by the surface pressure data obtained in the present experiment for correlation to the vorticity field results discussed above.

The correlation of the extent of the minimum value of the pressure coefficient with dimensionless frequency was reaffirmed and is shown in Figure 18. The fact that this variable is more closely correlated to dimensionless frequency rather than Reynolds number suggests that it is not related to maximum vorticity levels generated within a separated region, but is instead coupled to the geometry of the separation vortex. A comparison of the iso-vorticity contour maps and ensemble averaged surface pressure data does, in fact, confirm this suspicion.

A convenient method for effecting a comparison between these two entities is found by employing the y-coordinate averaged vorticity distribu-

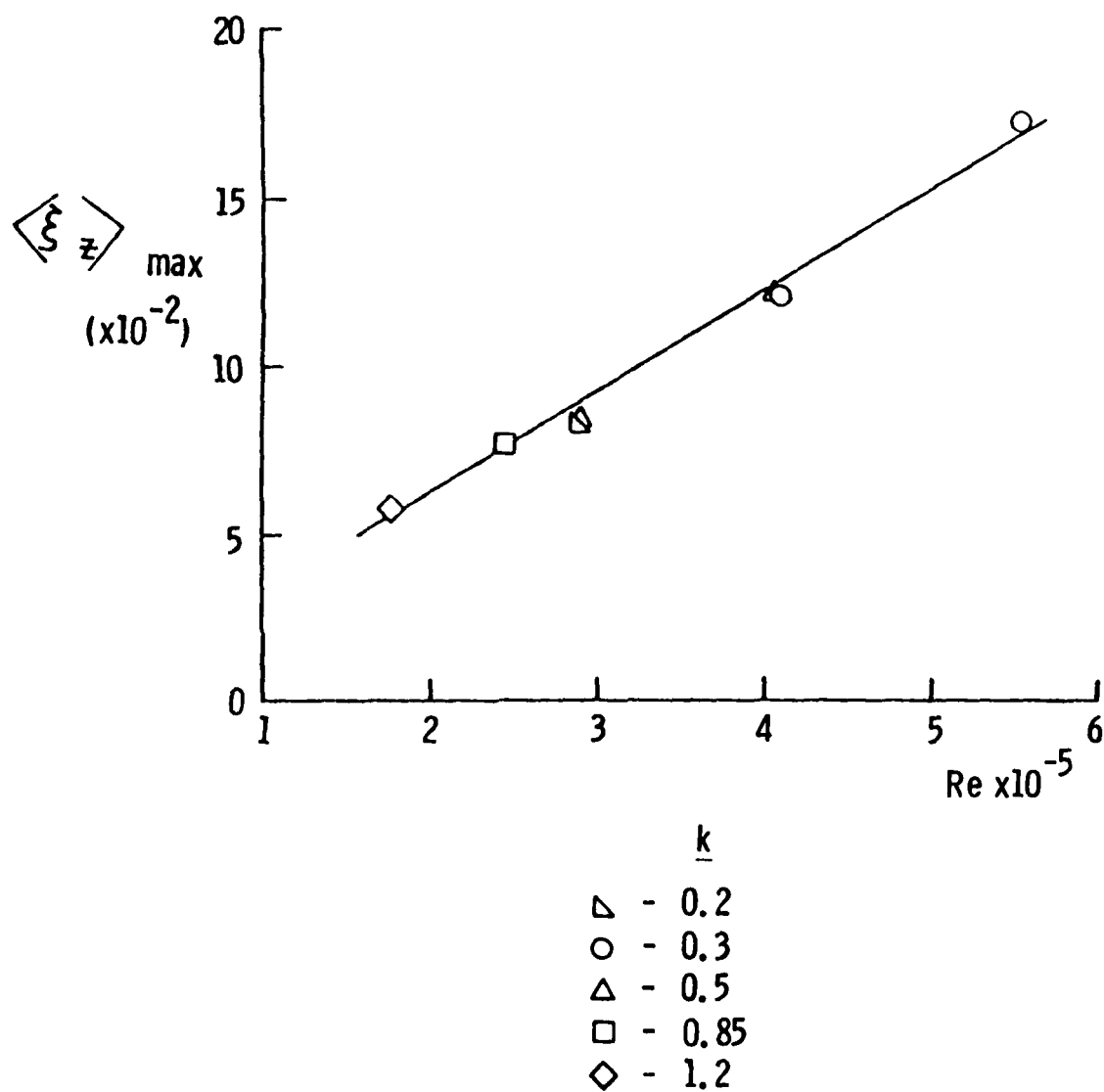
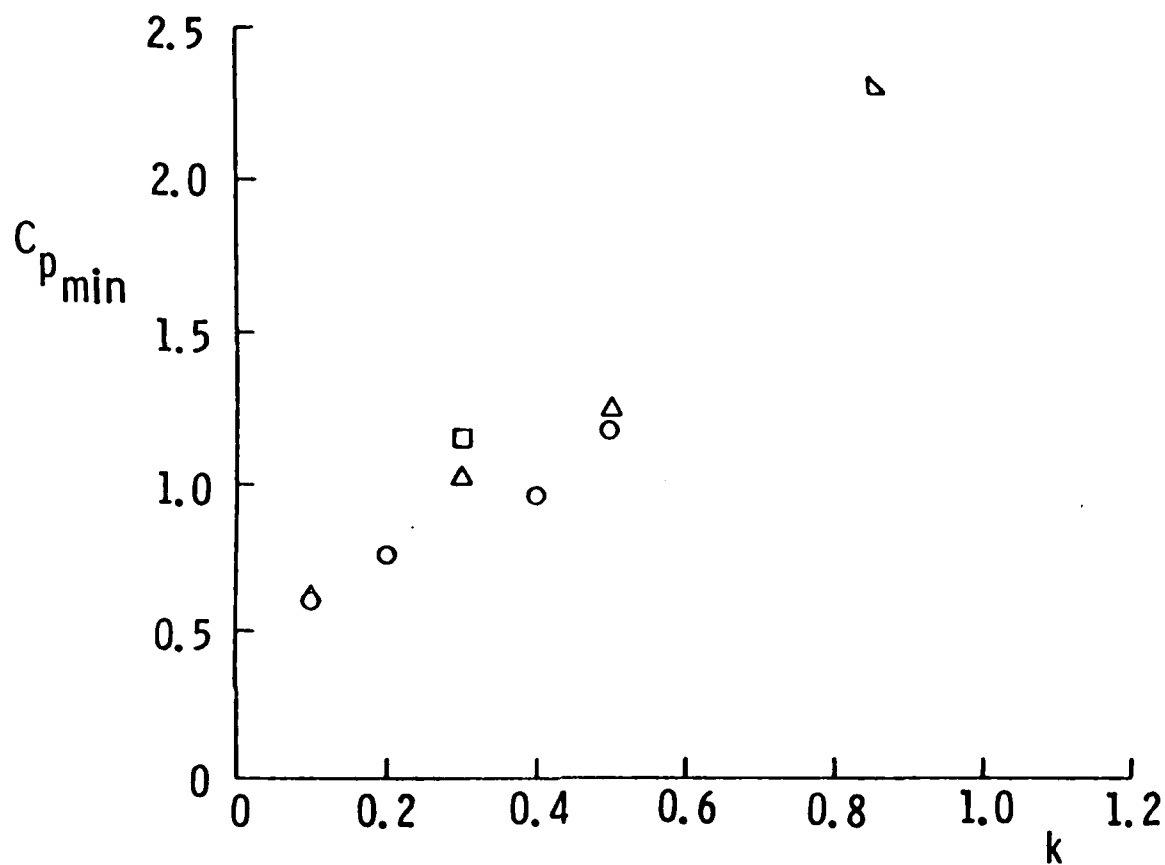


Figure 17. Maximum Value of Laterally-Averaged Vorticity as Function of Reynolds Number



Re $\times 10^{-5}$

∇ -2.46
 \circ -2.87
 \triangle -4.10
 \square -5.54

Figure 18. Minimum Pressure Coefficient Variation with Frequency

tions. The resultant comparison is provided for several different combinations of frequency and Reynolds number in Figure 19. The results are displayed for several select values of the phase angle.

Similarities in the separated region geometry on the upstroke are apparent. The location of the regions of maximum vorticity (indicative of the presence of the separation vortex) and the corresponding regions of local suction appear almost superimposed on one another. This correlation is especially close during the spoiler upstroke.

As the spoiler nears its maximum extension and during the subsequent downstroke portion of the cycle, the distribution of laterally-averaged vorticity is observed to nearly reach an equilibrium value. This can be explained by noting that vorticity leaving the measurement region through downstream convection is replaced by new vorticity generated at the spoiler tip (quasi-steady behavior). At the same time, the pressure field is observed to flatten out in a manner reminiscent of the roof-top distribution. As the spoiler retreats further, the flattened suction region is observed to decrease in magnitude while sustaining a constant level of vorticity. This apparent discrepancy is simply an indicator that, during the downstroke portion of the cycle, it is not the outer shear layer behavior which dominates the local surface pressure distribution, but rather flow effects occurring closer to the airfoil surface.

Again, concentrating on that part of the cycle during which the energetic vortex is formed, an appreciation can be developed for the correlation between pressure and flow field variables by comparing the extent of the separated region geometry as discussed above and the size of the suction region. This correlation is shown in Figure 20. The size of the suction region is again observed to grow in an almost linear manner coinciding with the extent of the shear layer vortex.

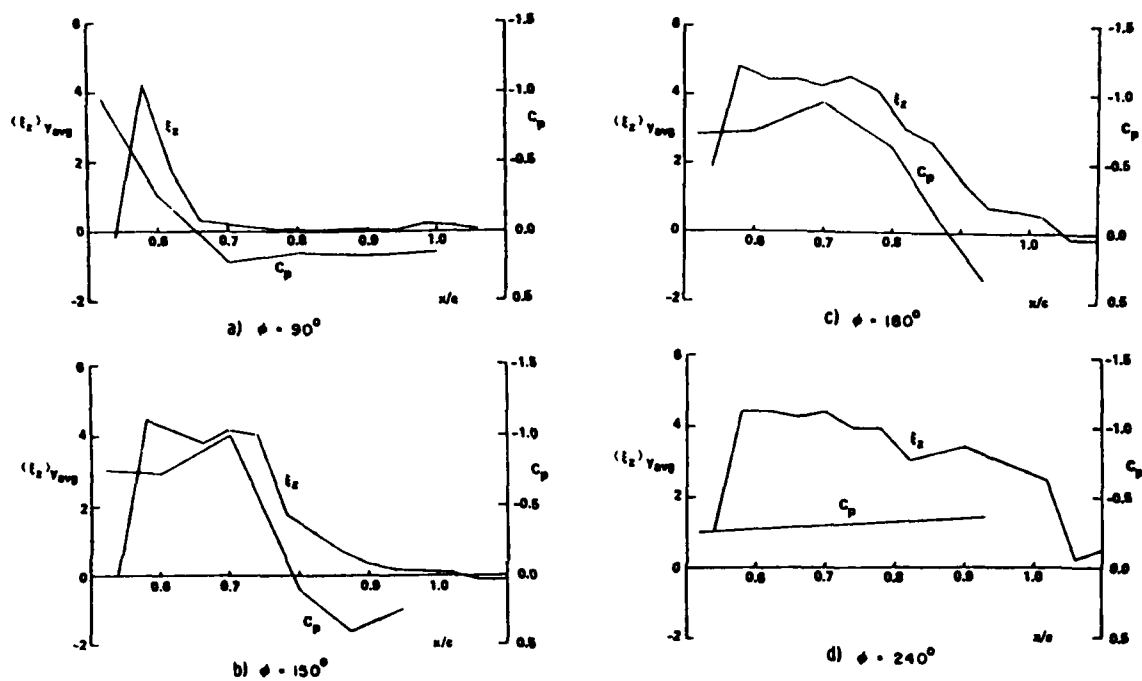
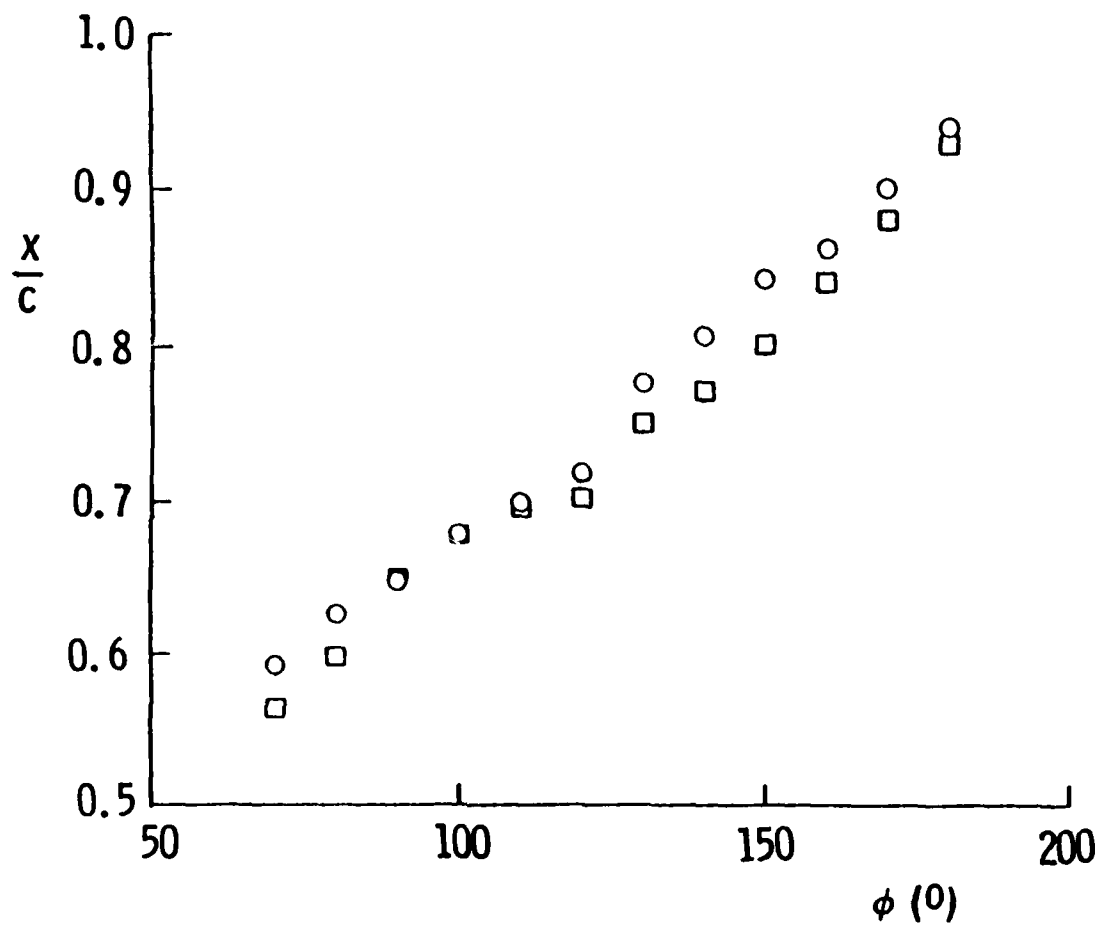


Figure 19. Comparison of Pressure Distribution and Laterally-Averaged Vorticity



○ - vorticity field

□ - pressure field

Re = 410,000, k = 0.5

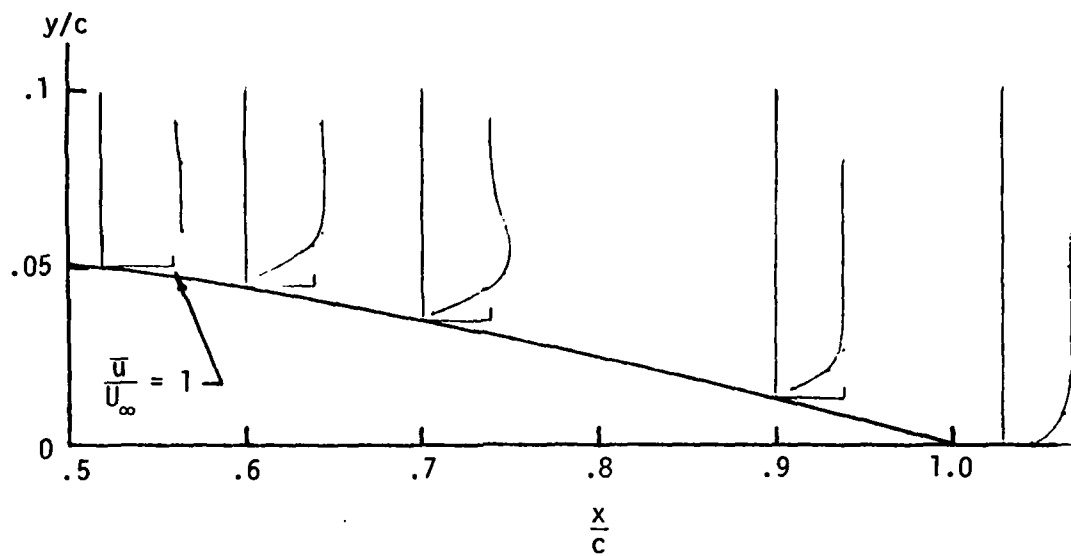
Figure 20. Length of Separation Zone - Comparison,
Re = 410,000, k = 0.5

G. Flow Near the Airfoil Surface

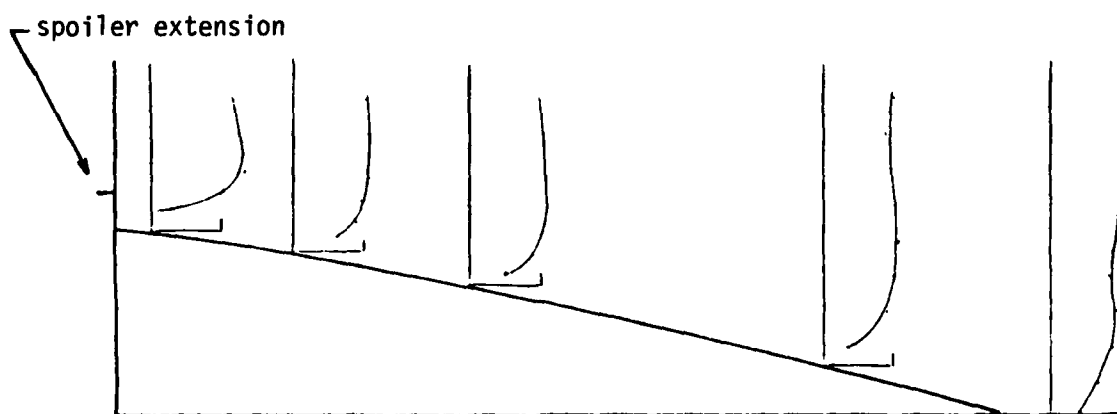
Inherent limitations of the hot-film anemometry measurement technique described previously severely restricted its use in regions near the airfoil and spoiler surfaces due to the existence of energetic flow reversal. It had been hoped that laser Doppler Velocimeter (LDV) measurements might be employed to compute the vorticity field in the near surface region to provide a complete map of this variable over the entire zone of separation. This was not accomplished, however, due to unusually low data rates at some locations which resulted in excessively long measurement times. The data rate problem was attributed to a number of factors including seed particle centrifuging during vortex passage, limited seed entrainment with the spoiler fully extended, and low signal-to-noise ratio due to reflected laser light at measurement locations very close to the surface.

As a result, unsteady velocity profiles were constructed from measurements at five chordwise locations including $x/c = 0.52$ (just behind the spoiler), 0.60, 0.70, 0.90, and 1.003. Examples of the mean freestream velocity component are shown in Figures 21 and 22 for two different values of the dimensionless frequency. These profiles provide a representative description of the near surface flow. Because a much less extensive set of measurement locations was required for this description than needed for a vorticity field representation, overall measurement times were minimized (3 hours, typical, for a single flow condition) resulting in improved stabilization of the wind tunnel environment over the entire length of the test.

Using dual Bragg cells to frequency shift the scattered laser signal,²⁰ flow reversal was measured in both magnitude and phase. The presence of energetic reversal is evident in Figures 21 and 22. Despite the limited series of measurements made in this region, and a restricted capability to

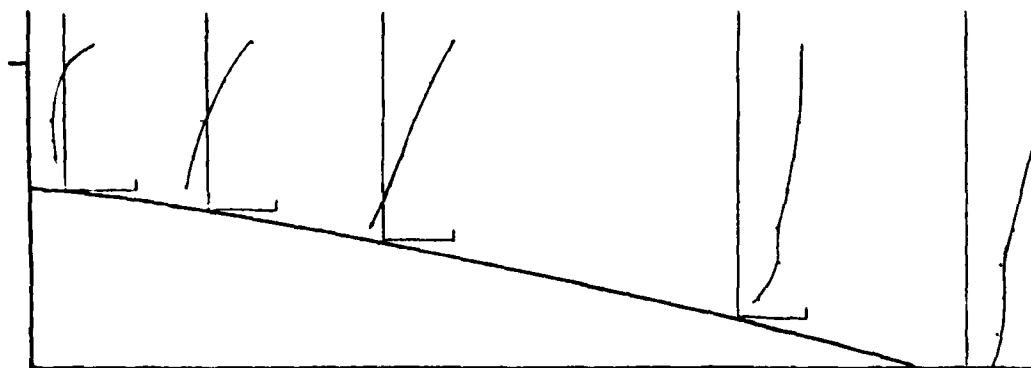


(a) $\phi = 0^\circ$

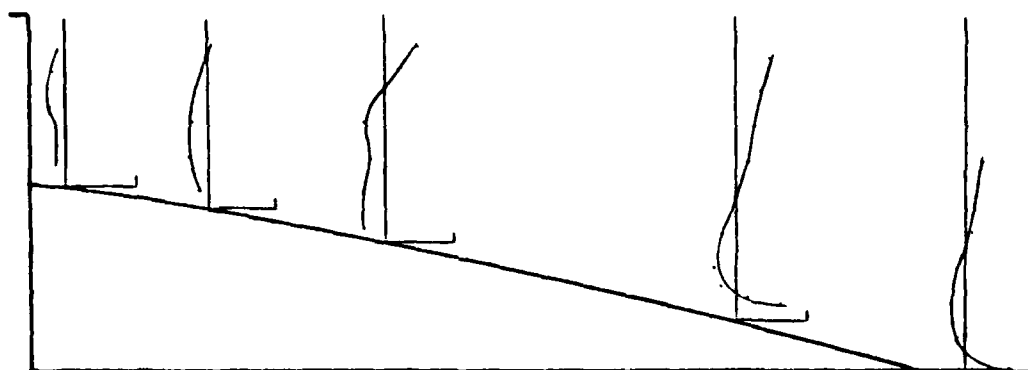


(b) $\phi = 60^\circ$

Figure 21. Freestream Velocity Component Profiles Obtained with Laser Doppler Velocimeter, $k = 0.2$, $U_\infty = 70$ ft/sec

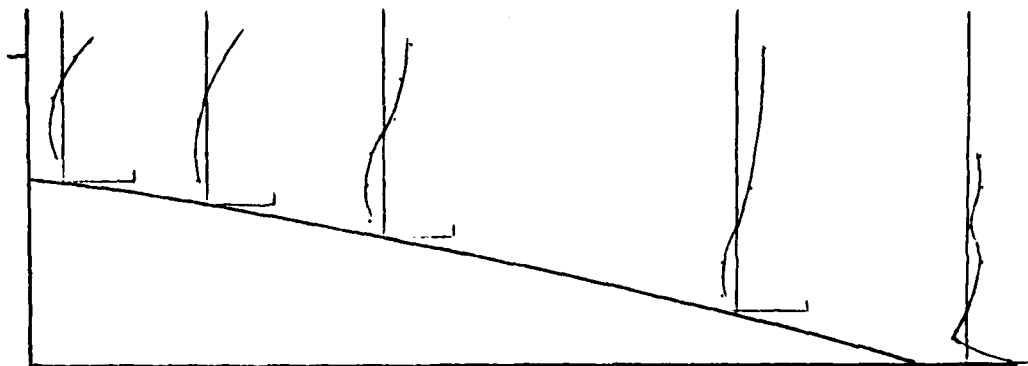


(c) $\phi = 120^\circ$

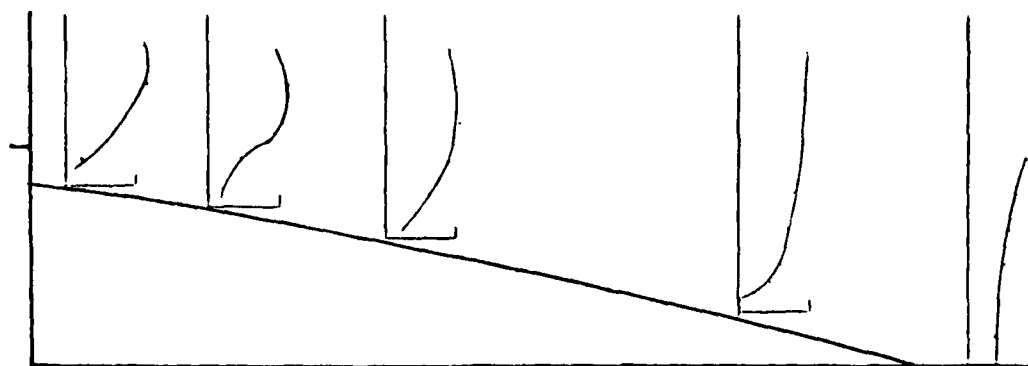


(d) $\phi = 180^\circ$

Figure 21 (cont.). Freestream Velocity Component Profiles Obtained with Laser Doppler Velocimeter, $k = 0.2$, $U_\infty = 70$ ft/sec

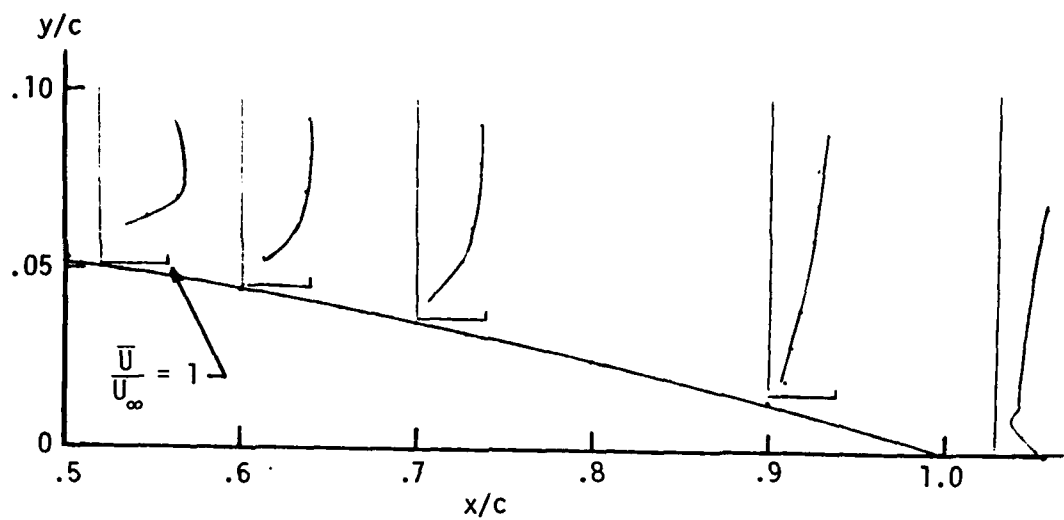


(e) $\phi = 240^\circ$



(f) $\phi = 300^\circ$

Figure 21 (cont.). Freestream Velocity Component Profiles Obtained with Laser Doppler Velocimeter, $k = 0.2$, $U_\infty = 70$ ft/sec

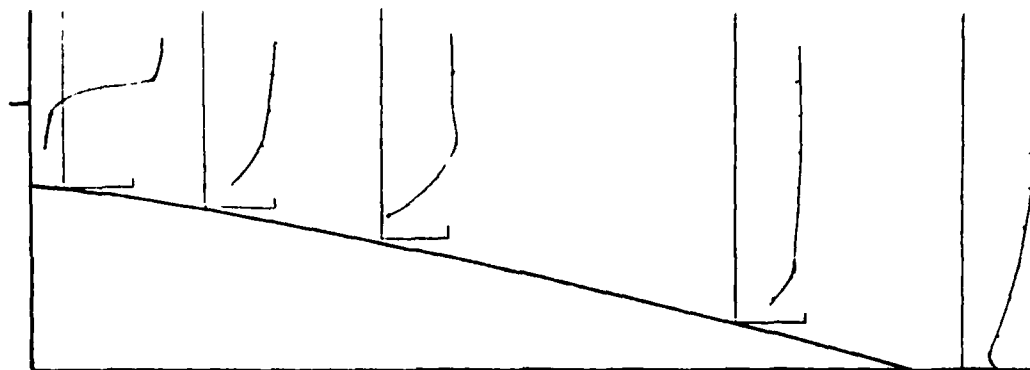


(a) $\phi = 0^\circ$

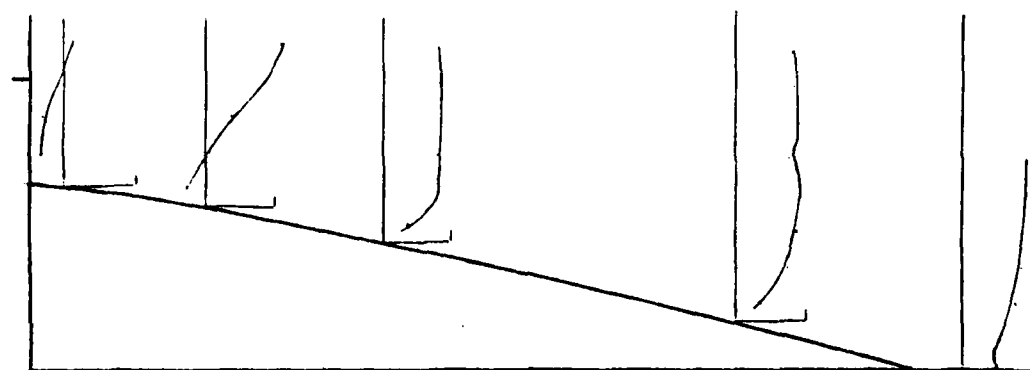


(b) $\phi = 60^\circ$

Figure 22. Freestream Velocity Component Profiles Obtained With Laser Doppler Velocimeter, $k = 0.85$, $U_\infty = 60$ ft/sec

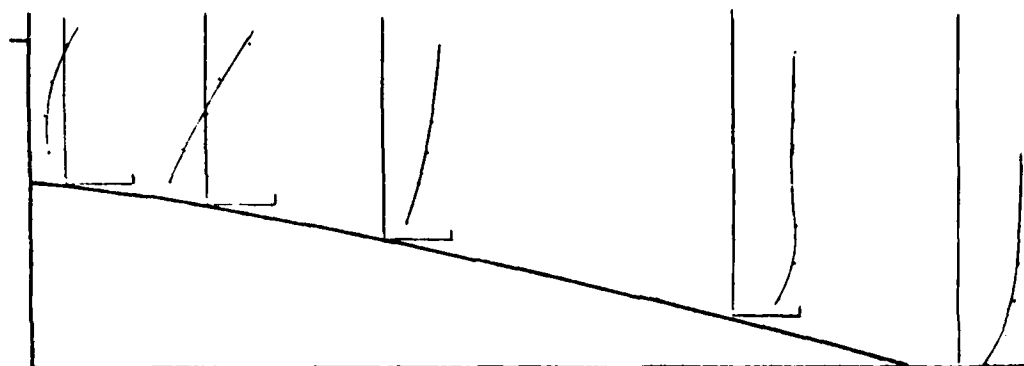


(c) $\phi = 90^\circ$

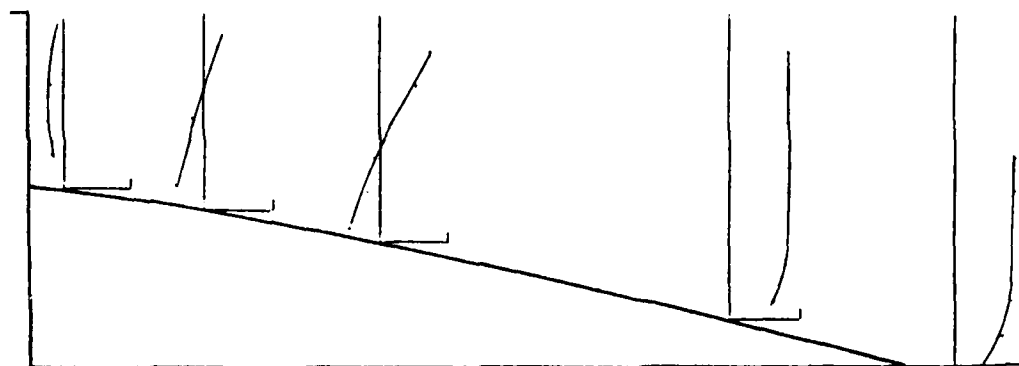


(d) $\phi = 120^\circ$

Figure 22 (cont.). Freestream Velocity Component Profiles Obtained with Laser Doppler Velocimeter, $k = 0.85$, $U_\infty = 60$ ft/sec

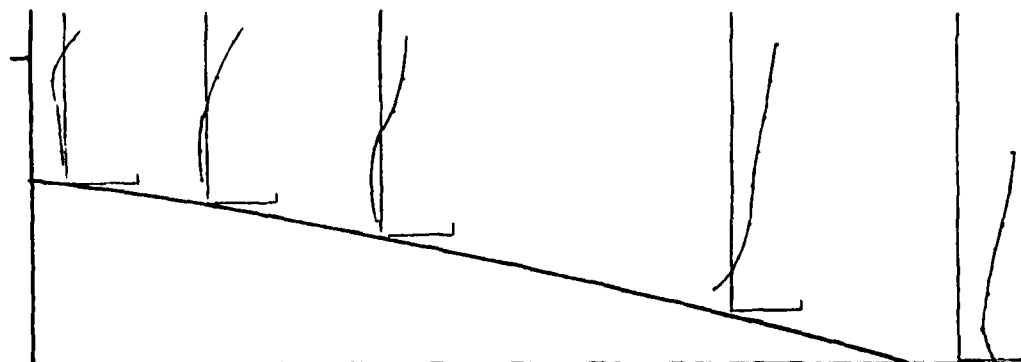


(e) $\phi = 150^\circ$

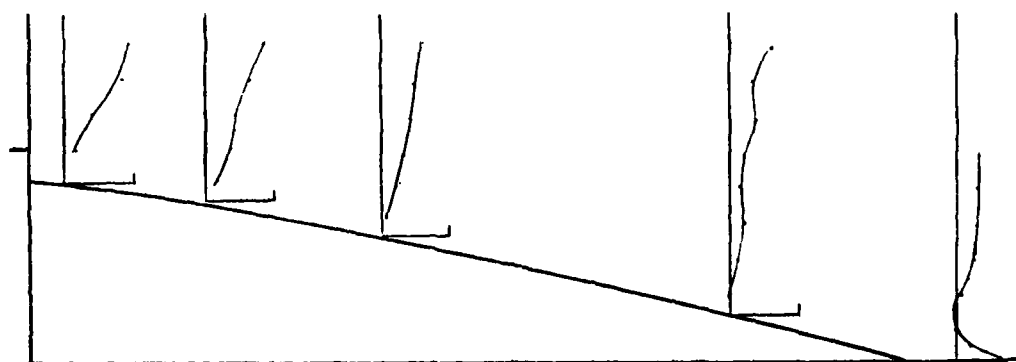


(f) $\phi = 180^\circ$

Figure 22 (cont.). Freestream Velocity Component Profiles Obtained with Laser Doppler Velocimeter, $k = 0.85$, $U_\infty = 60$ ft/sec



(g) $\phi = 240^\circ$



(h) $\phi = 300^\circ$

Figure 22 (cont.). Freestream Velocity Component Profiles Obtained with Laser Doppler Velocimeter, $k = 0.85$, $U_\infty = 60$ ft/sec

approach the model surface where reversal was prevalent, reversal magnitudes in excess of 55 percent of the freestream velocity were detected.

An alternative description of the extent of the separated region is suggested by the envelope within which flow reversal occurs. This region is depicted as a function of time in Figures 23 and 24 for a low frequency and a high frequency case, respectively. The phase lag dependence on frequency discussed previously is apparent but is not as obvious as with the mean vorticity field description. The quasi-steady behavior of the flow on the downstroke at low frequency can also be observed.

The extent of a lag in reversal is more evident using the reversal location phase histories shown in Figures 25 and 26 for the two frequencies. The peculiar behavior of the curves representing the profiles obtained nearest the spoiler is attributed to the existence of secondary eddies near the model/spoiler junction which were discussed previously.

The inability to achieve a more complete survey of reversal was limited, as indicated earlier, by restrictions in measuring close to the airfoil surface. Maximum reversal was observed to occur, almost without exception, at measurement locations closest to the airfoil surface independent of the phase angle. This, of course, suggests that the true reversal maxima lie even closer to the surface.

Lastly, a brief comment should be made regarding the comparison of hot-film and LDV measurements in regions of overlap - where both techniques provided "valid" data. The ability of the LDV system to accurately duplicate hot-film measurements in "well-behaved" flows has been discussed previously.²¹ Reasonable accuracy was also achieved in the unsteady cases as suggested in the example in Figure 27. During unsteady motion, however, the degree of agreement was found to be dependent on both spatial location and phase.

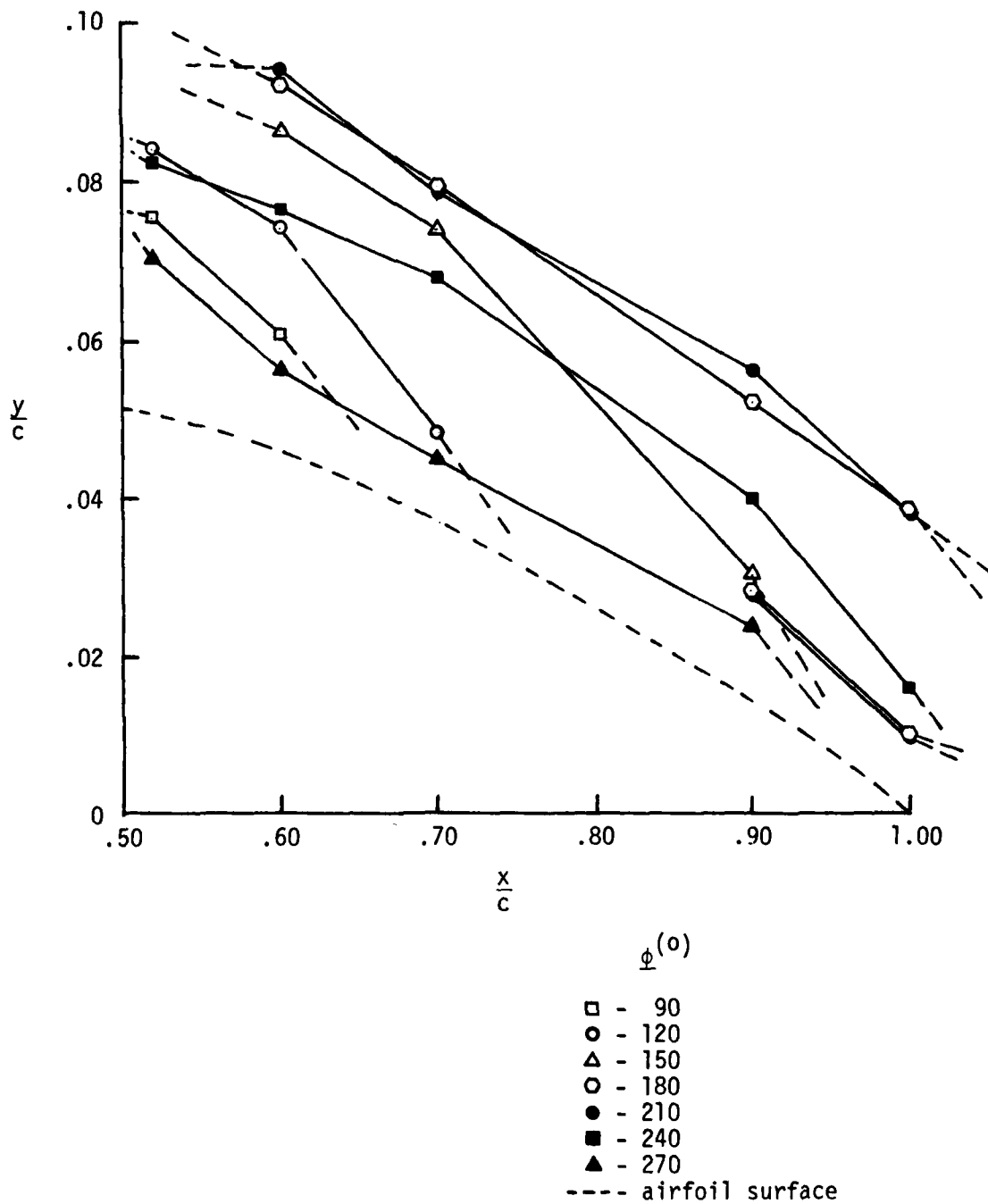


Figure 23. Freestream Velocity Component Flow Reversal Envelope, $k = 0.2$, $U_\infty = 70$ ft/sec

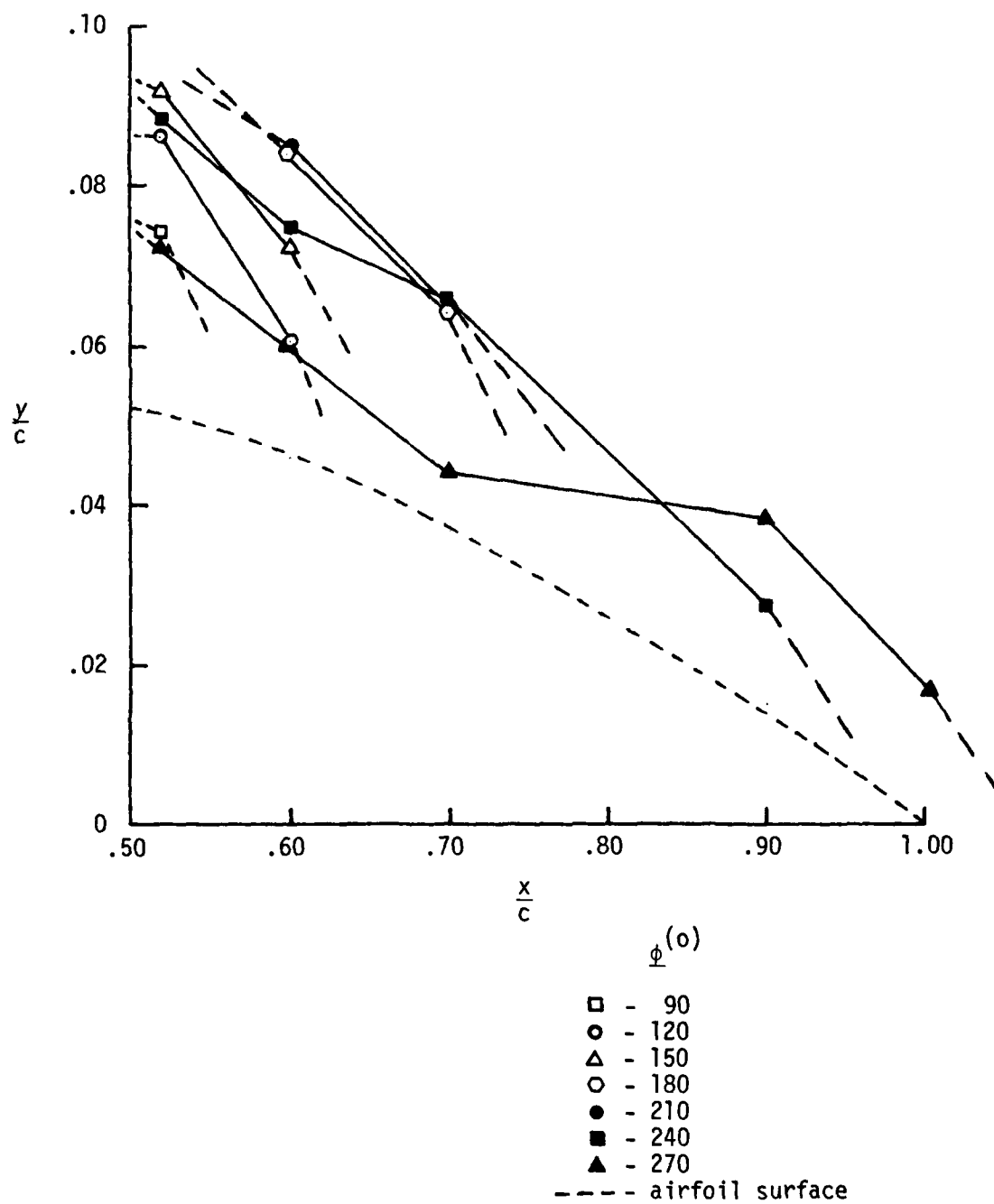


Figure 24. Freestream Velocity Component Flow Reversal Envelope, $k = 0.85$, $U_{\infty} = 60$ ft/sec

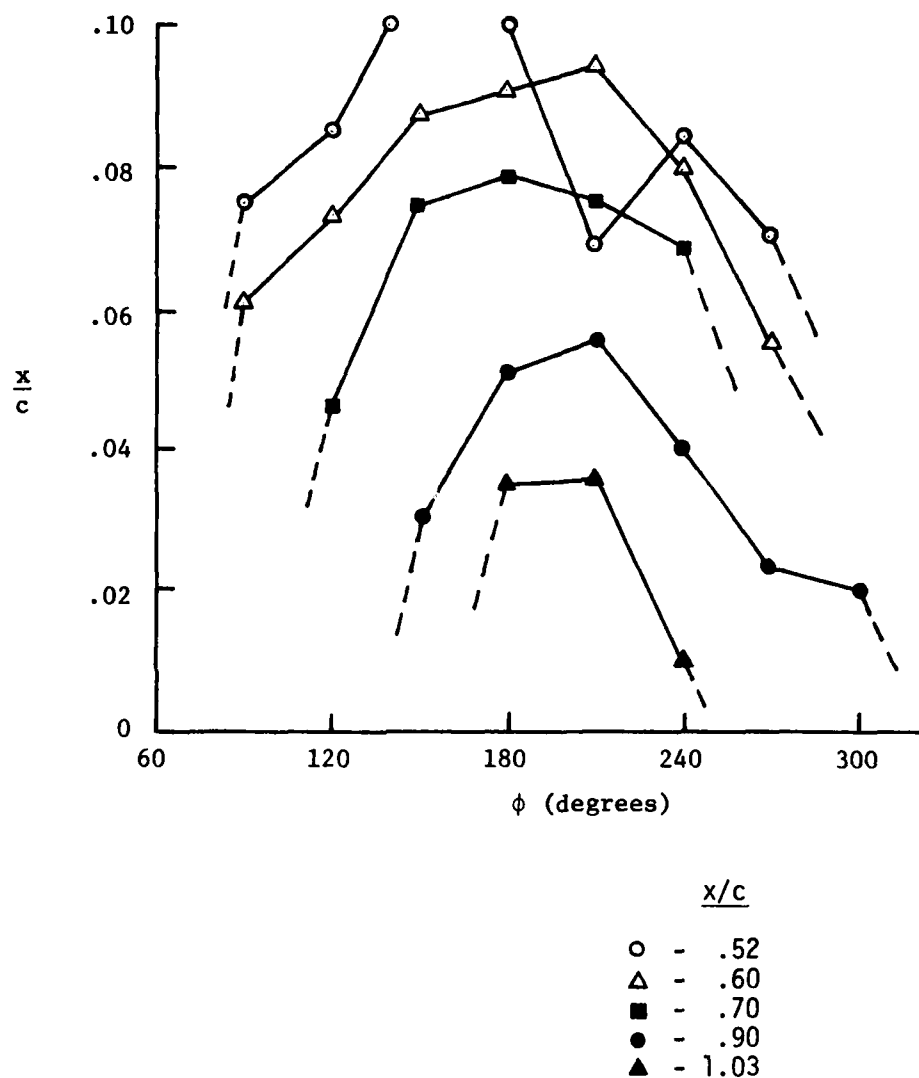


Figure 25. Freestream Velocity Component Flow Reversal - Phase History, $k = 0.2$, $U_{\infty} = 70$ ft/sec

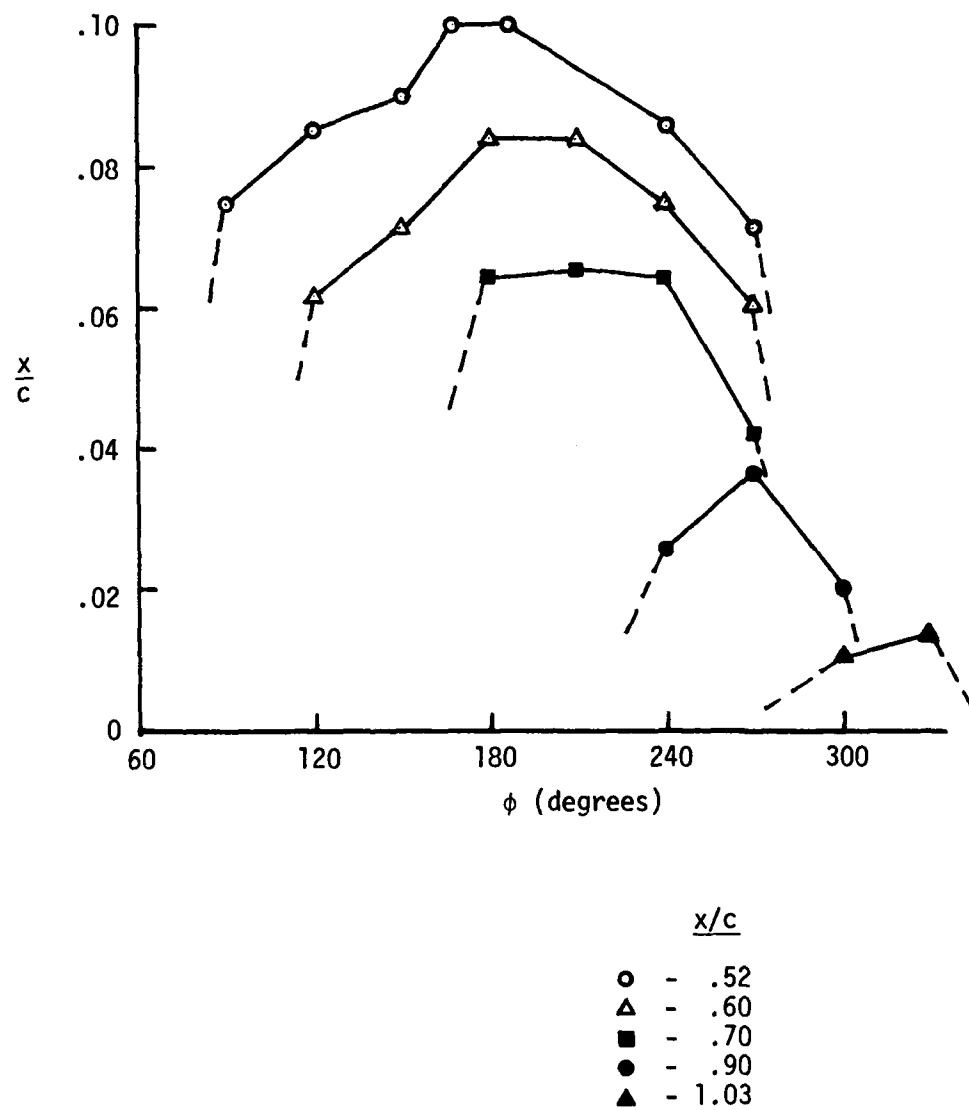


Figure 26. Freestream Velocity Component Flow Reversal - Phase History, $k = 0.85$, $U_{\infty} = 60$ ft/sec

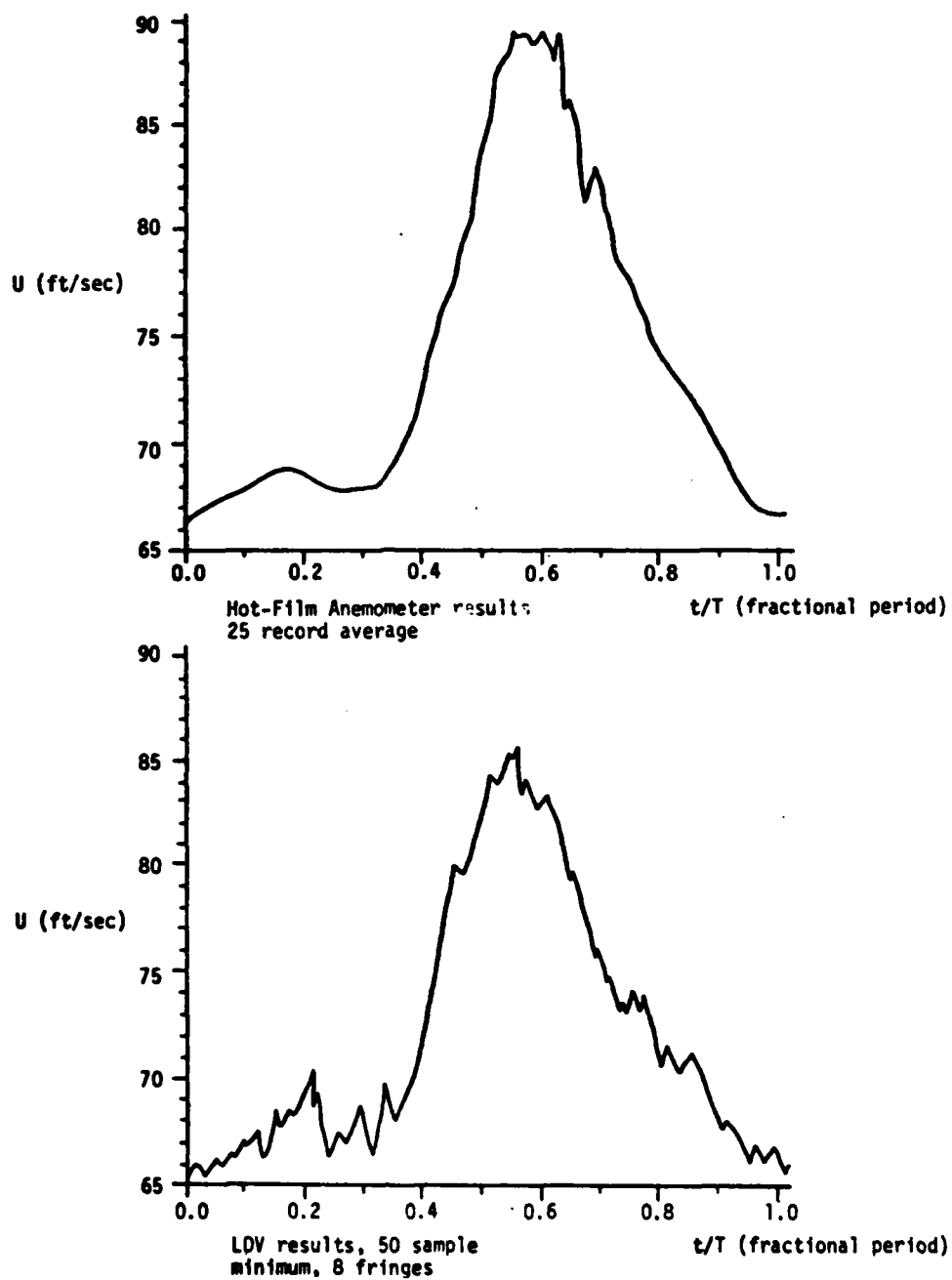


Figure 27(a). Comparison of Velocity Component Values in the Freestream Direction (Blue Beam)

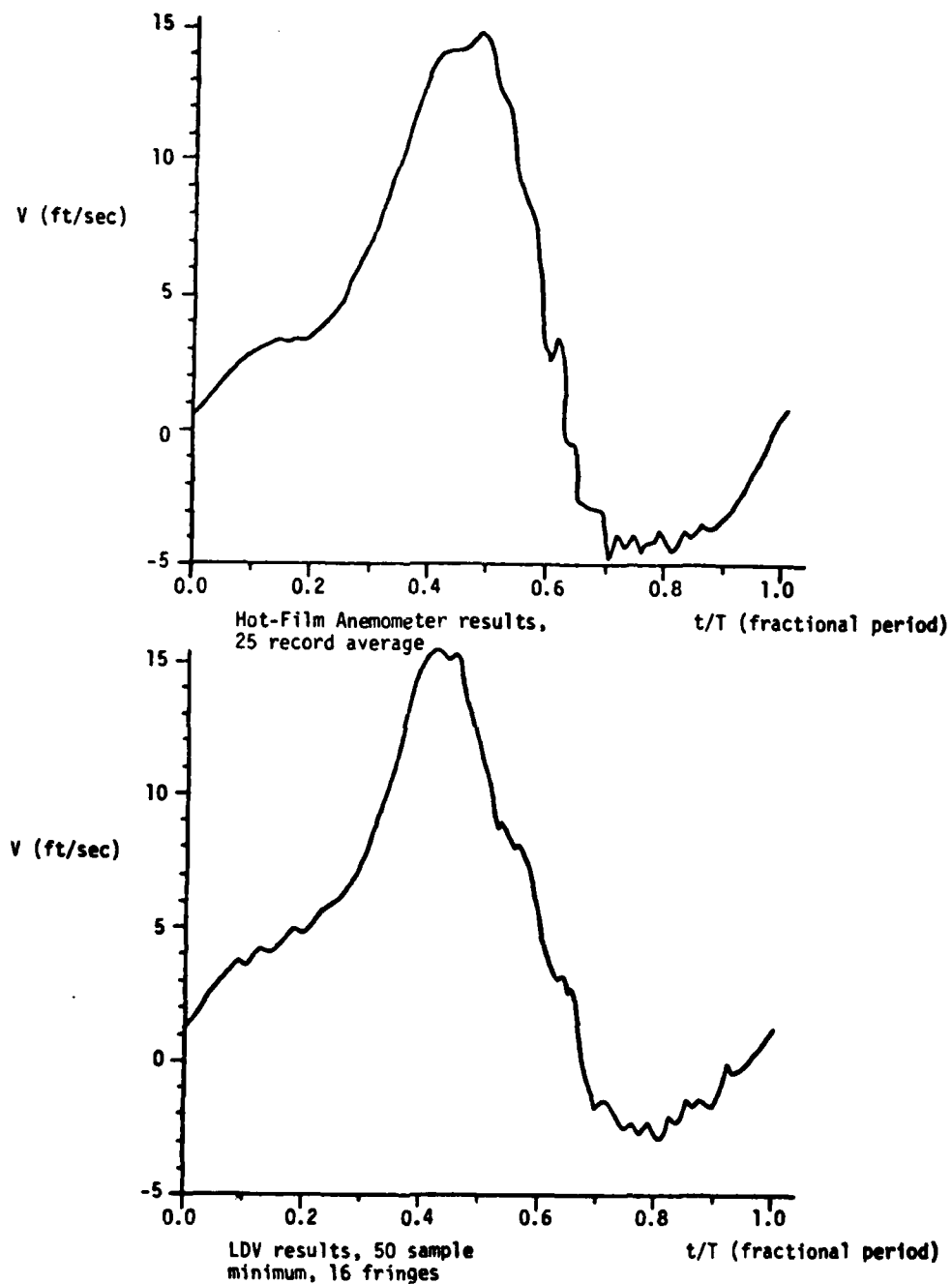


Figure 27(b). Comparison of Velocity Component Values
in the Downwash Direction (Green Beam)

H. Turbulence Intensities

Although the iso-vorticity contour maps provide an illustrative way to examine the detailed behavior of the evolution of the vortex, an alternative method for determining the phase lag characteristics involved in the growth of the separation zone can be achieved through an examination of the root-mean-square levels of fluctuating quantities like velocity with phase angle. The growth and sustenance of high rotation rates in the vortex interior tended to suppress higher levels of turbulence due to flow stability. Locally depressed values of these variables during the oscillation cycle can be correlated to determine the spatial and temporal passage of the more coherent regions of the vortex structure. Another purpose of these measurements was to establish the degree of accuracy of the mean flow data by determining the extent of variation of the local turbulence intensities.

Examples of the turbulence intensity distribution are provided in Figures 28 and 29 for a low frequency and high frequency case, respectively. Note that the value of the turbulence intensity is defined on the basis of the time-varying local mean value of the freestream-directed velocity component and not on the freestream velocity itself. This formulation provides a more realistic appraisal of the effects of turbulence than the more commonly accepted description. The degree of phase lag and its dependence on frequency are also apparent in these figures. The reduction in the strength and extent of the distribution during vortex passage at high frequency is also very apparent. The peak magnitudes observed in these measurements were also found to decrease with increasing values of k . This result is consistent with the concept of a more organized structure at higher frequencies. Peak values are also observed to increase in close proximity to and behind the spoiler. This is not due to increased magnitude

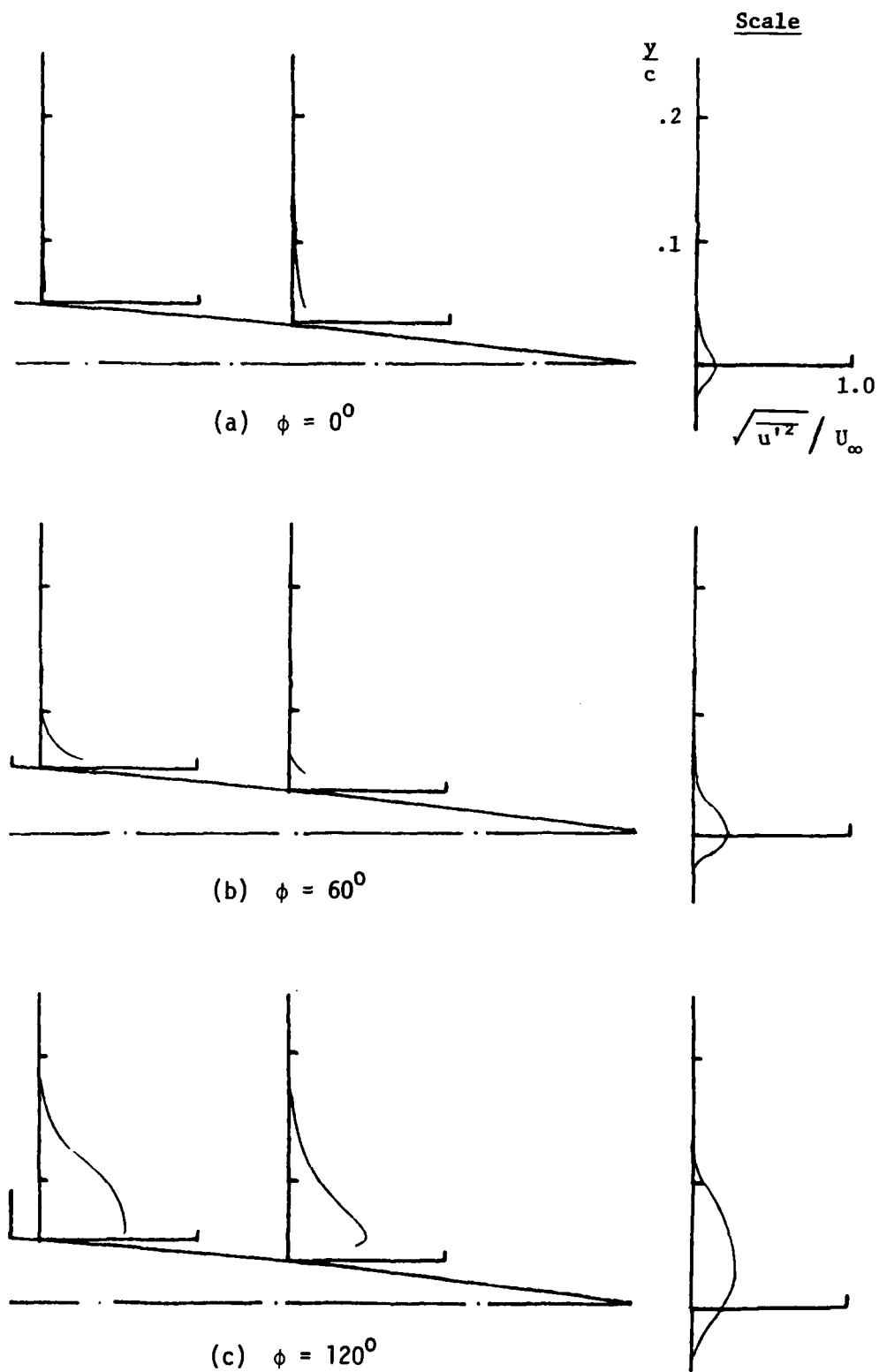
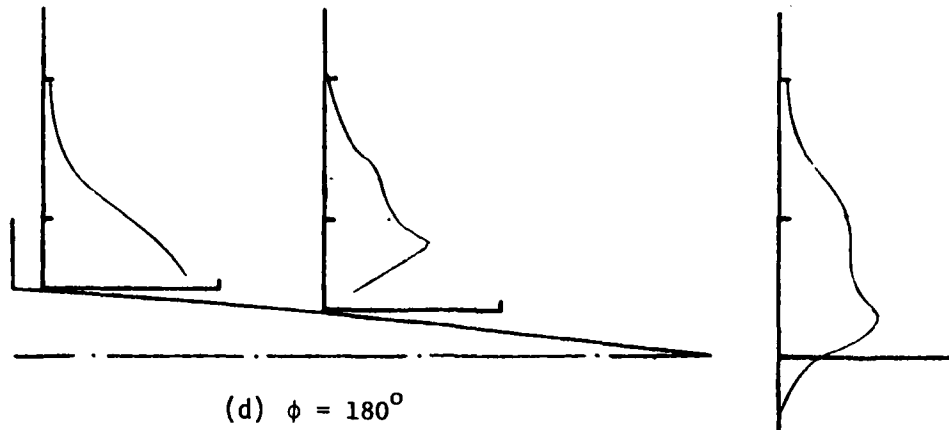
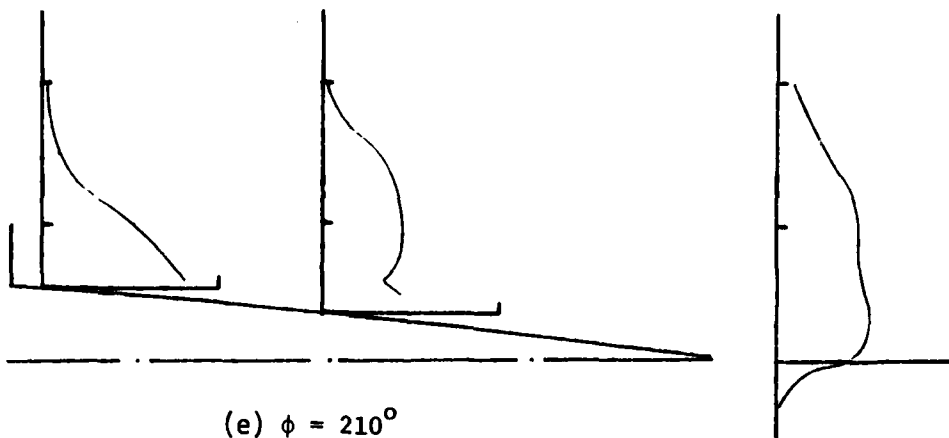


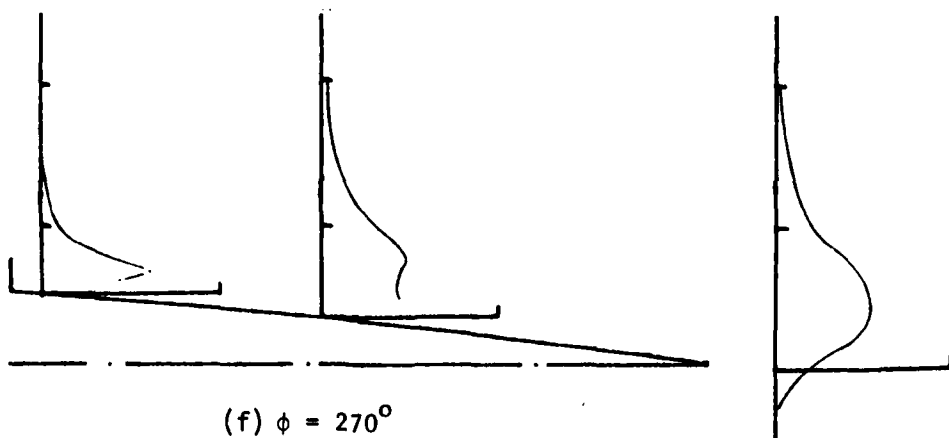
Figure 28. Freestream Velocity Component - Turbulence Intensity Profiles, $k = 0.2$, $U_\infty = 70$ ft/sec



(d) $\phi = 180^\circ$



(e) $\phi = 210^\circ$



(f) $\phi = 270^\circ$

Figure 28 (cont.). Freestream Velocity Component - Turbulence Intensity Profiles, $k = 0.2$, $U_\infty = 70$ ft/sec

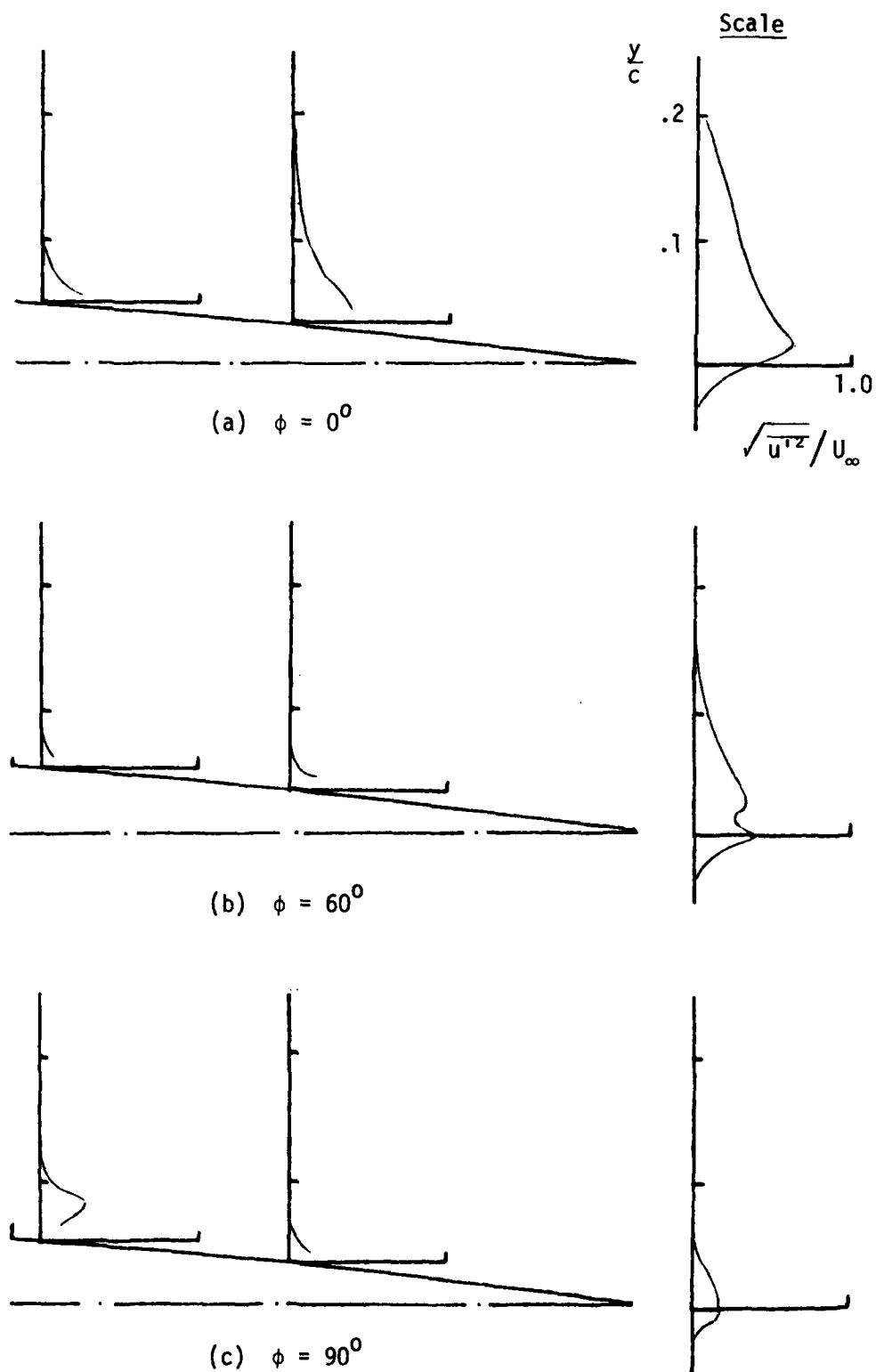


Figure 29. Freestream Velocity Component - Turbulence Intensity Profiles, $k = 0.85$, $U_\infty = 60$ ft/sec

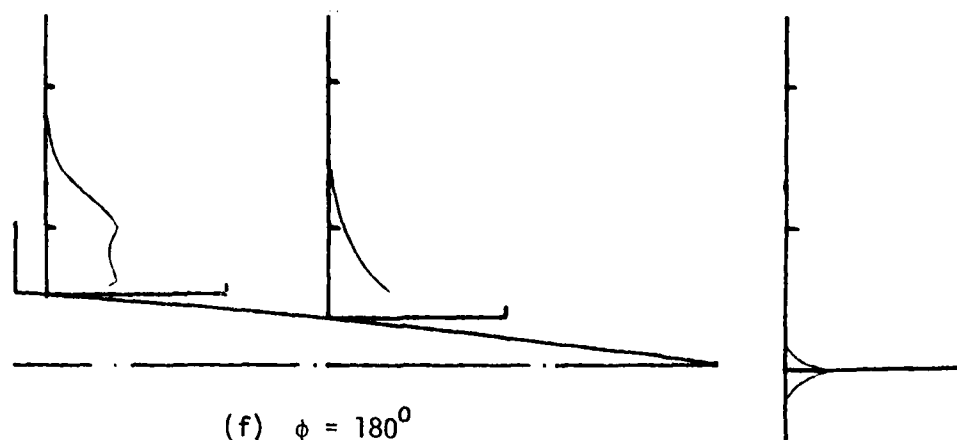
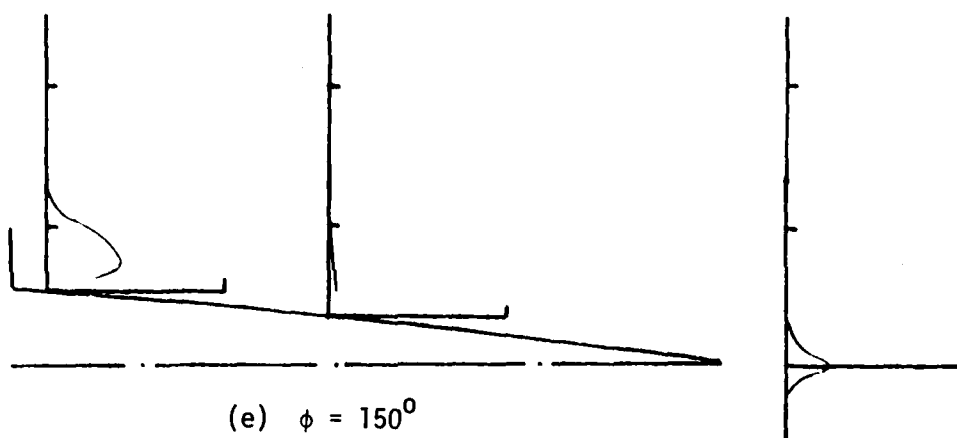
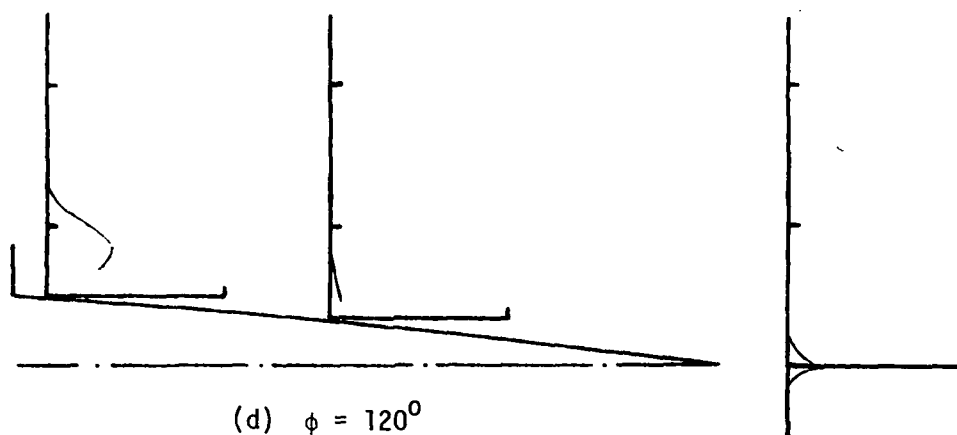


Figure 29 (cont.). Freestream Velocity Component - Turbulence Intensity Profiles, $k = 0.85$, $U_\infty = 60$ ft/sec

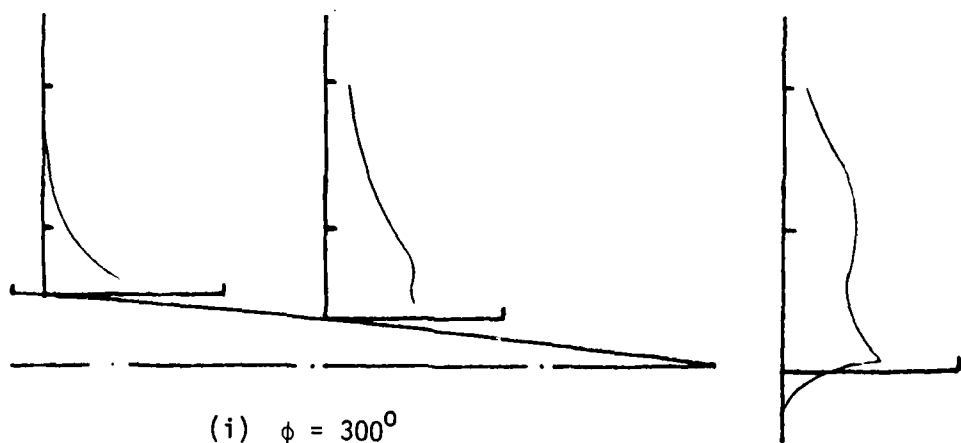
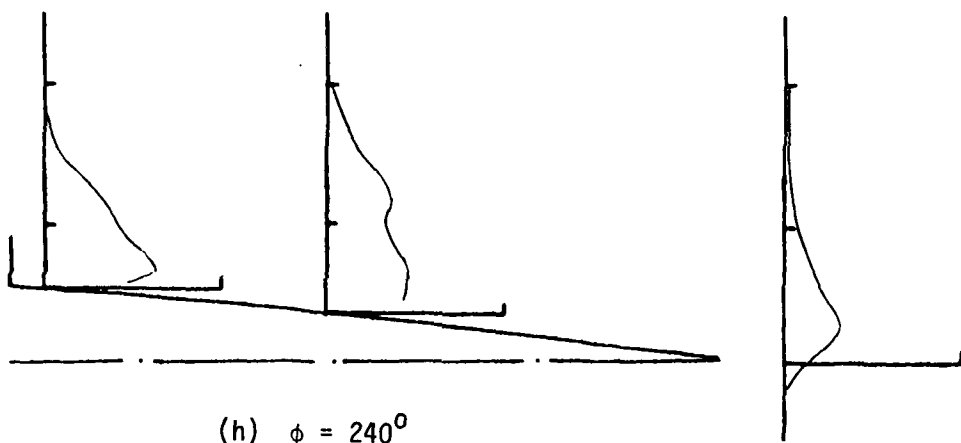
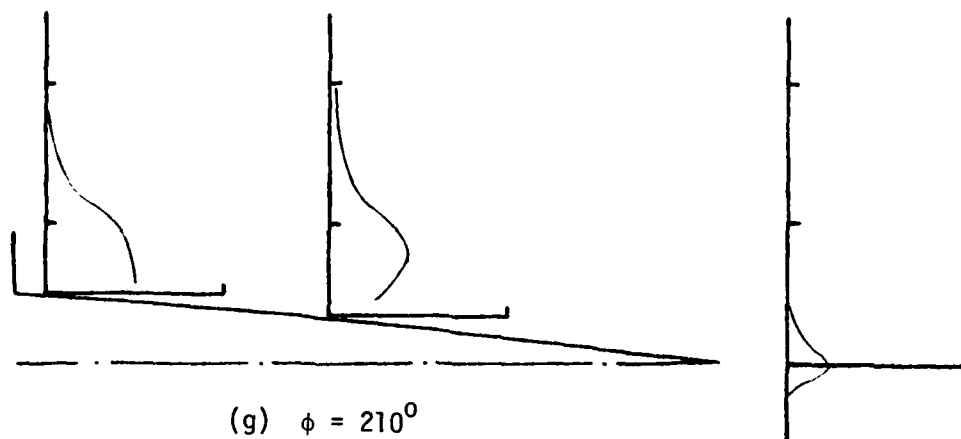


Figure 29 (cont.). Freestream Velocity Component - Turbulence Intensity Profiles, $k = 0.85$, $U_\infty = 60$ ft/sec

in turbulent velocity values but rather decreased levels of the normalizing mean velocity component.

The extent of phase lag is also evident in a graphical description of the location of the local maximum values of turbulence intensity as shown in Figures 30 and 31.

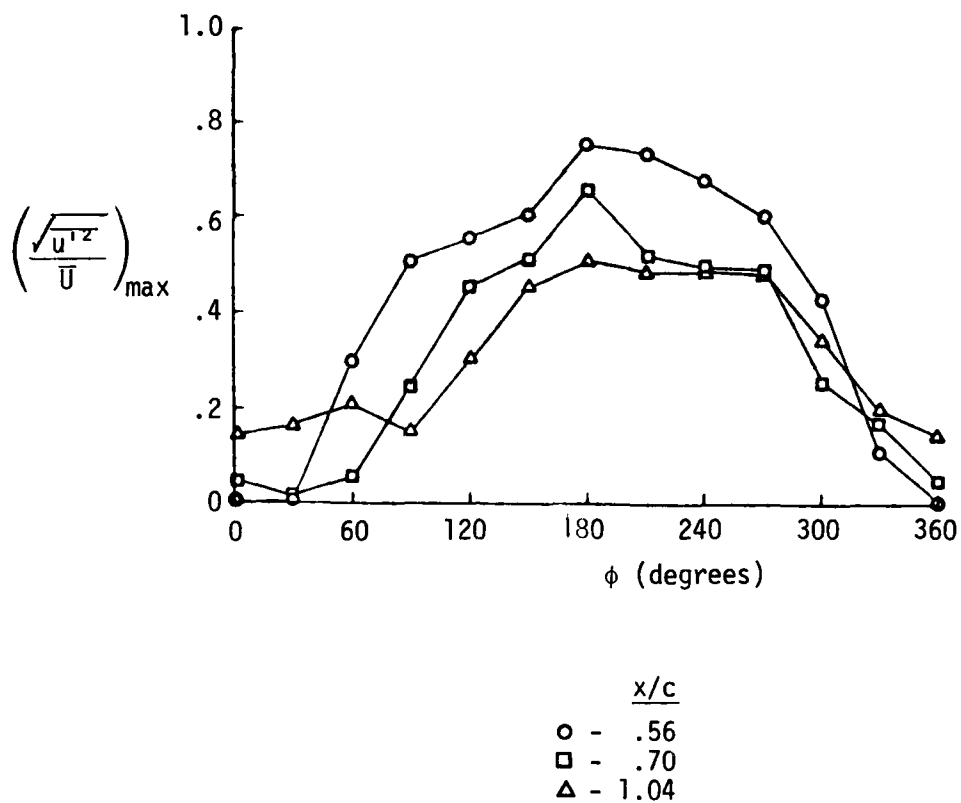


Figure 30. Maximum Turbulence Intensities - Phase Histories, $k = 0.2$, $U_{\infty} = 70$ ft/sec

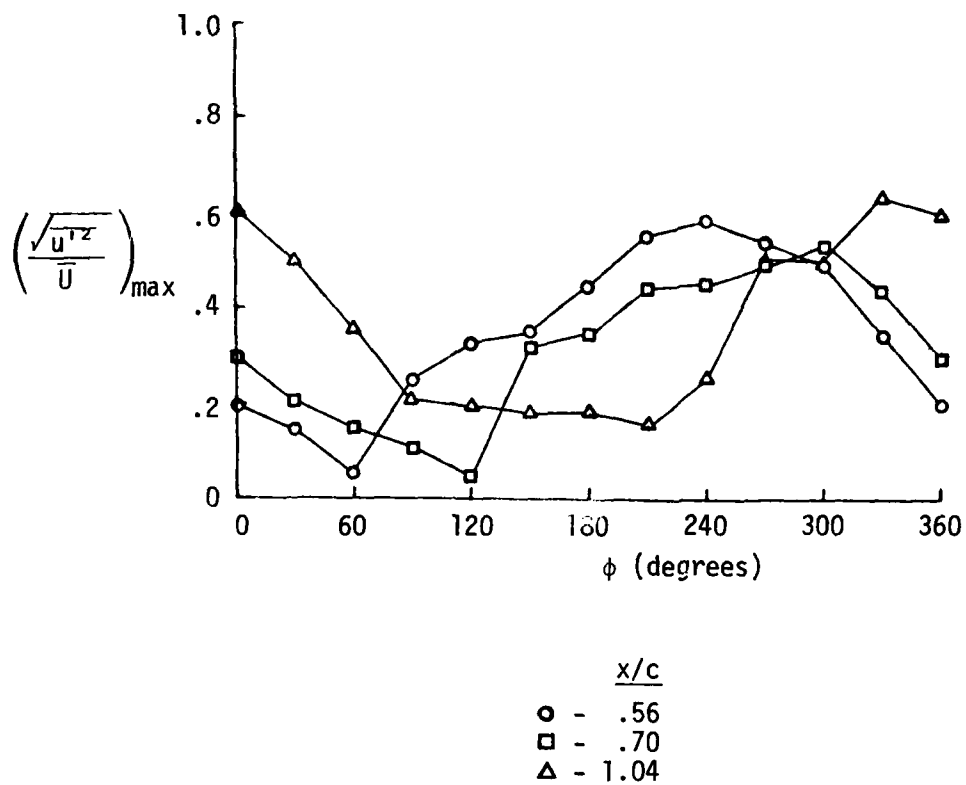


Figure 31. Maximum Turbulence Intensities - Phase Histories, $k = 0.85$, $U_{\infty} = 60$ ft/sec

SUMMARY

The unsteady separated region generated over the upper surface of the airfoil by harmonic spoiler oscillations is identified as a dynamically evolving vortex-like structure bearing a strong resemblance to the one encountered in the dynamic stall flowfield. This description has been confirmed using measurements of the time-varying mean and turbulent velocity and vorticity fields near the model surface and in the outer shear layer. It has also been verified through hydrogen-bubble flow visualization tests in a low speed water tunnel.

For high Reynolds number flow and dimensionless frequencies between zero and unity, the structure is observed to be attached to the spoiler (at least during the upstroke portion of the cycle) while it elongates in the freestream direction. Its growth is observed to be directly proportional to the time of evolution and not closely correlated to the non-linear spoiler motion. The dimensionless characteristic growth rate of the vortex is observed to be directly proportional to the square root of the dimensionless frequency.

The primary source of vorticity following the structure's formation is the action of the accelerated freestream over the tip of the moving spoiler. The geometric characteristics of the separation vortex are related to the extent of the suction region during the spoiler upstroke. The magnitude of the suction peak appears to be correlated with the laterally averaged vorticity distribution, and not with the maximum peak vorticity levels found in the shear layer.

The vorticity field characterizing the outer shear layer and the corresponding surface pressure distribution were not closely correlated during the downstroke part of the cycle. The mechanisms which influence

the behavior of the surface pressure distribution in these instances are believed to be related to flow conditions nearer the surface.

Energetic flow reversal near the airfoil surface has been confirmed using laser Doppler velocimetry techniques and is correlated with the passage of the separation vortex as determined through measurements of the outer shear layer.

ACKNOWLEDGEMENTS

The research described above was sponsored by the Frank J. Seiler Research Laboratory (AFSC) under project/task 2307-F1. The authors gratefully acknowledge the efforts of Mr. Carl Geddes, Instrument Maker, whose exceptional craftsmanship is responsible for the quality of the experimental apparatus. Captain James M. Lind provided extensive assistance in the development of data acquisition hardware and software required for the completion of these experiments. The Department of Aeronautics greatly assisted by providing the use of their wind tunnel facility.

The authors also wish to express their appreciation and gratitude to the personnel of the U.S. Army Aeromechanics Laboratory, Research and Technology Laboratories (AVRADCOM) located at the Ames Research Center, for their assistance in conducting the water tunnel flow visualization experiments. Dr. Ken McAlister, Dr. Larry Carr, Dr. W. J. McCroskey, and Mr. Art Cocco are to be especially commended. We gratefully acknowledge the support provided by the NASA photographic unit, especially Mr. Joe March.

Our thanks are also extended to Ms. Donna Weiss for her painstaking efforts in the preparation of this manuscript.

REFERENCES

1. Chang, P. K., Separation of Flow, 1st Ed., London, Pergamon Press, 1970.
2. Viegas, J. R. and Coakley, T. J., "Numerical Investigation of Turbulence Models for Shock Separated Boundary-Layer Flows," AIAA 15th Aerospace Sciences Meeting, Los Angeles, CA, Paper No. 77-44, January 1977.
3. Trilling, L., "Oscillating Shock Boundary-Layer Interaction," Journal of the Aeronautical Sciences, Vol. 25, May 1958, pp. 301-304.
4. Lighthill, M. J., "On the Weis-Fogh mechanism of lift generation," Journal of Fluid Mechanics, Vol. 60, Pt. 1, 1973, pp. 1-17.
5. Maxworthy, T., "Experiments on the Weis-Fogh mechanism of lift generation by insects in hovering flight, Pt. 1, Dynamics of the 'fling'," Journal of Fluid Mechanics, Vol. 93, Pt. 1, July 1979, pp. 47-63.
6. Ham, N. D., "Aerodynamic Loading on a Two-Dimensional Airfoil during Dynamic Stall," AIAA Journal, Vol. 6, No. 10, October 1968, pp. 1927-1934.
7. Crimi, P. and Reeves, B. L., "A Method for Analyzing Dynamic Stall," AIAA 10th Aerospace Sciences Meeting, San Diego, CA, Paper No. 72-37, January 1972.
8. Ericsson, L. E. and Reding, J. P., "Analytic Prediction of Dynamic Stall Characteristics," AIAA 5th Fluid and Plasma Dynamics Conference, Boston, MA, Paper No. 72-682, June 1972.
9. McCroskey, W. J., Carr, L. W. and McAlister, K. W., "Dynamic Stall Experiments on Oscillating Airfoils," AIAA 13th Aerospace Sciences Meeting, Pasadena, CA, Paper No. 75-125, January 1975.
10. McAlister, K. W., Carr, L. W. and McCroskey, W. J., "Dynamic Stall Experiments on the NACA 0012 Airfoil," NASA Technical Paper 1100, January 1978.
11. Mehta, U. B., "Dynamic Stall of an Oscillating Airfoil," AGARD Paper No. 23, Symposium on Unsteady Aerodynamics, Ottawa, Canada, 26-28 September 1977.
12. McCroskey, W. J., "Some Current Research in Unsteady Fluid Dynamics," 1976 Freeman Scholar Lecture, Transactions of the ASME, Journal of Fluids Engineering, March 1977, pp. 8-39.
13. McCroskey, W. J., "Introduction to Unsteady Aspects of Separation in Subsonic and Transonic Flow," AGARD Lecture Series No. 94, Three-Dimensional and Unsteady Separation at High Reynolds Numbers, Paper No. 6, February 1978.

14. Barnes, C. S., "A Developed Theory of Spoilers on Aerofoils," ARC Current Paper 887, July 1965.
15. Newman, B. G., "The Reattachment of a Turbulent Boundary-Layer Behind a Spoiler," Aeronautical Research Laboratories, Report A64, Melbourne, Australia, 1949.
16. Lang, J. D., "The Dynamics of a Growing Separated Region on an Airfoil," Frank J. Seiler Research Laboratory Technical Report, SRL-TR-75-0005, February 1975.
17. Lang, J. D. and Francis, M. S., "Interaction of an Oscillating Control Surface with an Unsteady Separated Region," Journal of Aircraft, Vol. 13, No. 9, September 1976, pp. 687-694.
18. Lang, J. D. and Francis, M. S., "Dynamic Loading on an Airfoil due to a Growing Separated Region," AGARD Symposium on Prediction of Aerodynamic Loading, Paper No. 26, NASA Ames Research Center, CA, September 1976.
19. "Subsonic and Trisonic Wind Tunnel Facilities," Department of Aeronautics, U.S. Air Force Academy, 1977.
20. Kadlec, R. A., Sparks, G. W., Jr., Francis, M. S., "The Development of a Laser-Doppler Velocimetry System for Unsteady Separated Flow Research - Preliminary Results," Frank J. Seiler Research Laboratory Report SRL-TR-78-0010, October 1978.
21. Sparks, G. W., Jr., Retelle, J. P., Jr., Keesee, J. E., Francis, M. S., Lind, J. M., "A Laser Doppler Velocimeter System to Investigate Unsteady Flow Separation," ISA 25th International Instrumentation Symposium, Anaheim, CA, May 7-10, 1979.
22. Olsen, J. H. and Liu, H. T., "The Construction and Operation of a Water Tunnel in Application to Flow Visualization Studies of an Oscillating Airfoil," NASA CR-114696, May 1973.
23. McAlister, K. W. and Carr, L. W., "Water Tunnel Experiments on an Oscillating Airfoil at $Re = 21,000$," NASA Tech Memo 78446, March 1978.
24. Francis, M. S., Kennedy, D. A. and Butler, G. A., "Technique for the measurement of spatial vorticity distributions," Review of Scientific Instruments, Vol. 49, No. 5, May 1978, pp. 617-623.
25. Keesee, J. E., Francis, M. S. and Lang, J. D., "A Technique for Vorticity Measurement in Unsteady Flow," AIAA Journal, Vol. 17, No. 4, April 1979, pp. 387-393.
26. Francis, M. S., Lang, J. D. and Keesee, J. E., "Water Tunnel Measurements of Unsteady Separation," Frank J. Seiler Research Laboratory Report, SRL-TR-78-0011, December 1978.
27. Tennekes, H., Lumley, J. L., A First Course in Turbulence, MIT Press, 1st ed., Cambridge, MA, 1972, p. 127.